A phase-time-path-difference approach for online wave direction and wave number estimation from measured ship motions in zero and forward speed using a single inertial measurement unit

Johann A. Dirdal [a,*], Roger Skjetne [b], Jan Roháč [c], Thor I. Fossen [a]

[a] *Department of Engineering Cybernetics, Norwegian University of Science and Technology (NTNU), NO-7491 Trondheim, Norway*
[b] *Department of Marine Technology, Norwegian University of Science and Technology (NTNU), NO-491 Trondheim, Norway*
[c] *Department of Measurement, Faculty of Electrical Engineering, Czech Technical University in Prague, Prague, Czech Republic*

ARTICLE INFO

ABSTRACT

This study investigates the potential capability of a relatively new and unexplored signal-based approach for shipboard wave estimation. The approach uses the phase-time-path-differences (PTPDs) from an array of shipboard sensors to uniquely resolve the wave propagation direction and wave number. We derive a kinematic PTPD model accounting for forward vessel speed and assess its theoretical foundation to model the sensor delays on a rigid body. The forward-speed PTPD model is structurally equivalent to the zero-speed model considered in previous works, thus retaining the same observability results provided by a noncollinear array of a minimum of three sensors. Moreover, based on the outlined theory and PTPD model, we propose a methodology to estimate the main wave propagation direction and wave number online by employing a fast Fourier transform (FFT), an unscented Kalman filter (UKF), and a rigid-body measurement transformation based on a *single* inertial measurement unit (IMU). Provided that the vessel in question can be considered a rigid body, a single IMU is sufficient to obtain the desired wave quantities instead of three IMUs, as initially proposed in our previous work. Additionally, our methodology incorporates a novel frequency threshold to avoid distorted wave components caused by the effect of vessel filtering. The performance of our PTPD method is evaluated on data collected from a wave tank and full-scale experiments involving a vessel with zero and non-zero forward speed. The results show very good agreement with the reference wave values reported from a commercial wave radar and wave buoys operating in proximity to the vessel, indicating that our proposed method is competitive with existing wave measurement technology in terms of accuracy and online performance while being cheap, easy to install, flexible, and robust against environmental influences.

1. Introduction

Accurate information about the propagation direction and frequency characteristics of ocean waves is essential for various maritime activities. Ship captains rely on this data to chart safer and more efficient routes, reducing wave-related impacts and potential danger. Notably, the risk of wave-induced rolling – particularly parametric rolling – is a chief concern, capable of causing cargo loss and, in extreme cases, vessel capsizing. Additionally, in dynamic positioning (DP) applications, knowing the wave direction aids in aligning the vessel with the wave disturbance (a process known as weathervaning (Kim and Kim, 2014)) to minimize control forces and increase stability and safety onboard. In the context of DP, the wave frequency also plays a crucial role for filtering out oscillatory motions from

entering the feedback loop, thereby improving fuel efficiency and reducing actuator wear (Fossen, 2021). Moreover, knowledge about the wave propagation direction and wave number/frequency can, in general, serve as valuable input to several existing sea state estimation frameworks (e.g., Brodtkorb et al. (2018)) to improve the quality of wave estimations.

The physical distance between a pair of sensors situated on the ocean surface induces a delay between the wave elevation measurements recorded by them. This delay manifests itself as either a *phase*, *time*, or *path* difference (PTPD), which depends on the distance between the sensors, the propagation speed of the waves passing through the bodies containing the sensors, and the angle at which the waves approach them. Many studies have investigated the capabilities of using

---

the PTPDs between a group of sensors to determine the main wave propagation direction (Esteva, 1976, 1977; Fernandes et al., 1988, 2000; Draycott et al., 2015, 2016, 2018; Luo et al., 2020). However, some practical drawbacks of these works are that they do not consider the wave number – although it can also be resolved from the same data (Donelan et al., 1996; Fernandes et al., 2001) – and they rely on a fixed stationary array of sensors, confining wave estimation to a specific geographical site. A more practical approach is to bring the sensors onboard a vessel and use the measured PTPDs to resolve the wave direction (and wave number) at any desired location, stationary or while moving. However, only a few studies have considered a shipboard PTPD approach (Fu et al., 2011; Udjus, 2017; Heyn et al., 2017; Dirdal et al., 2022). Hence, the capabilities of such an approach still need more exploration in the context of shipboard wave estimation (i.e., the field concerned with inferring statistics about ocean waves from sensor measurements taken onboard a ship) by considering more realistic wave conditions.

Most of the research on shipboard wave estimation is dominated by approaches based on the wave buoy analogy (Waals et al., 2002; Tannuri et al., 2003; Nielsen, 2006; Pascal et al., 2009; Nielsen, 2017a; Brodtkorb et al., 2018). However, a significant practical drawback of such approaches is that they rely on ship-dependent transfer functions known as response amplitude operators (RAOs), which should be determined for each ship using various hydrodynamic codes. Although some recent research activities have addressed this issue by proposing strategies for more accurate RAO tuning (Nielsen et al., 2021; Mounet et al., 2022), such transfer functions are not trivial to obtain and generally subject to many uncertainties. The fact that RAOs are transfer functions also limits the theoretical validity of these model-based approaches to linear systems, which for ships at sea, is only considered valid for mild and moderate wave conditions. In contrast, signal-based approaches (e.g., PTPD) are not constrained to any particular wave climate and require no ship information, rendering them considerably more practical as wave estimation is done directly from sensor measurements. However, only a handful of signal-based techniques are commercially available and hinge on wave radars and/or laser altimeters, which are expensive, sensitive to environmental influences, and challenging to install without expert help. Although shipboard wave estimation techniques based on machine learning (Mak and Düz, 2019; Duz et al., 2019; Han et al., 2022; Mittendorf et al., 2022) are also considered signal-based, they require ship-specific datasets, thus restricting generalization to other vessels.

The PTPD approach, on the other hand, is inherently signal-based and, when coupled with inertial measurement units (IMUs) as primary sensory devices, alleviate many of the practical concerns listed above by being inexpensive, robust against environmental impact, and easy to install; without requiring any detailed ship information. Despite the many advantages, current PTPD approaches using IMUs (Udjus, 2017; Heyn et al., 2017; Dirdal et al., 2022) have only been tested with stationary model ships in wave tanks involving regular waves. Consequently, the PTPD approach with IMUs needs further investigation in more realistic wave conditions and forward speed to solidify their potential. In this regard, extending the present PTPD framework to account for forward vessel speed will significantly improve the practical feasibility of the approach, which to our knowledge, is yet to be considered.

Accurate measurements of the PTPDs are a prerequisite for successful wave estimation using the PTPD approach. In general, the PTPDs are susceptible to several sources of error, including sensor noise, sensor imperfections (e.g., nonlinear sensitivity character and non-orthogonality and misalignment between inner sensitive axes), inexact sensor locations and alignments when installed, low data sampling rate, and modeling uncertainties. Although some of the literature above has acknowledged some of these errors, only one study (Dirdal et al., 2022) has attempted a quantitative analysis in the context of shipboard IMUs. However, the latter study does not account for modeling errors caused by mismatches in the PTPD dynamics when measured on a vessel (rigid

body) rather than on the sea surface. The magnitude of such errors may be significant and can explain some of the deviations observed in the wave estimation results of the latter study. Hence, it is important to consider the properties of a rigid body in the theoretical foundation of the PTPD approach for shipboard sensors.

A practical disadvantage of current PTPD approaches is that they require much hardware in the form of multiple IMUs and cables that should be connected, synchronized in time, and distances between them measured before they can be applied. When multiple sensors are considered, a reduction in the sensors' sampling rate from their maximum possible value is usually required to accommodate the increased information load associated with multiple simultaneous measurements. However, decreasing the sensor sampling rate will inadvertently affect the accuracy of the measured PTPDs (Dirdal et al., 2022), which, in turn, will affect wave estimation quality. It is, however, possible to reduce the amount of hardware to a *single* IMU by employing a rigid body measurement transformation to generate the remaining (virtual) IMU measurements. Although such a measurement transformation is not novel (Zappa et al., 2001; Kjerstad and Skjetne, 2016), no work has yet attempted to use this transformation to facilitate PTPD wave estimation.

In general, implementing a methodology based on the PTPD concept requires two main procedures: estimating the PTPDs from the sensor measurements and estimating the wave direction and wave number from the PTPDs. Although there are numerous ways of realizing such a methodology, a practically feasible methodology must leverage two essential factors: accuracy and real-time/online estimation performance—the focal points of most studies considering shipboard wave estimation. However, another factor that needs to be addressed is the lowpass wave filtering characteristics of a ship, which occur whenever the waves passing through it are sufficiently short. When this happens, the waves become distorted by the vessel, and the measured vessel responses no longer accurately reflect the true wave conditions. Although many works have shown awareness of this problem (Nielsen, 2007, 2008; de Souza et al., 2018; Nielsen et al., 2019; Nielsen and Dietz, 2020), most of the discussions are qualitative, with the main remedy being to consider other responses measured by additional complementary sensors, which are less affected by filtering (Nielsen, 2008; de Souza et al., 2018). A quantitative measure is introduced in a recent study (Dirdal et al., 2022) showing when the effect of vessel filtering is likely to occur based on the length and breadth dimensions of the vessel and its orientation relative to the incoming waves. However, there currently does not seem to exist a procedure for avoiding the distorted portion of the measured vessel responses caused by high-frequency waves, which is inevitable for any irregular sea as some of the constituent wave components are naturally high in frequency.

In this study, we extend previous findings by the following contributions. First, the theoretical foundation of the PTPD approach is rigorously assessed. From this assessment, the circumstances under which the PTPD approach may be used to model the phase difference between a pair of sensors on a rigid body are carefully identified. These conditions are also verified experimentally from data collected during wave tank experiments with a model ship in regular and irregular waves. Second, we derive a new PTPD model for vessels with short-time constant forward speed and verify it experimentally on data collected from forward speed experiments in a wave tank involving regular and irregular waves. This PTPD model is structurally equivalent to our previous zero-speed model and, hence, observable for a minimum of three noncollinear-spaced sensors. Third, based on the theory outlined, we propose a methodology for resolving the wave propagation direction and wave number online, which comprises an FFT, UKF, and a rigid-body measurement transformation based on a single IMU. Our methodology incorporates a novel frequency threshold derived from the length and breadth dimensions of the vessel to avoid distorted wave components due to the filtering effect. Finally, we assess the capabilities of our proposed method in practice by considering data
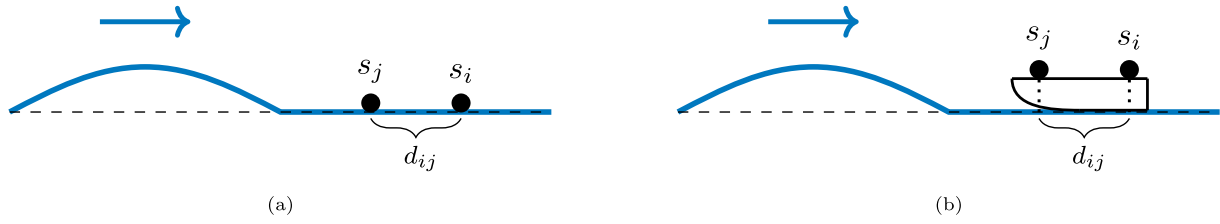
Fig. 1. Two sensors denoted s_i and s_j situated on (a) the ocean surface and (b) a rigid body. The distance between the sensors is labeled d_{ij}.
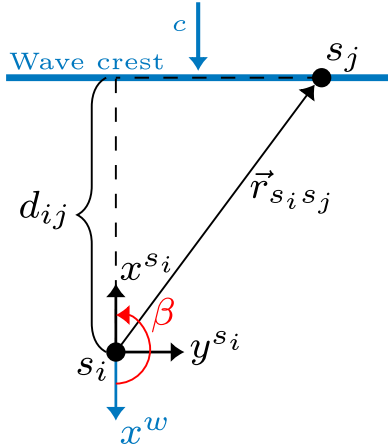

Fig. 2. A bird's-eye view of two sensors $\{s_i\}$ and $\{s_j\}$ positioned on the sea surface with a long-crested regular wave (shown in blue) passing through them with speed c. The wave should travel a distance d_{ij} to get from $\{s_j\}$ to $\{s_i\}$, which causes a constant delay between the wave elevation time series recorded in each sensor. The distance d_{ij} is expressed in the wave tangent frame $\{w\}$ with axes (x^w, y^w, z^w) and is attached to the (arbitrarily chosen) reference sensor $\{s_i\}$. The x^w axis points in the same direction as the propagating waves, z^w points upwards (out of the page), and y^w completes the right-handed coordinate system (not shown, but coincides with y^{s_i}). The relative wave direction β is defined as the counterclockwise angle from x^w to x^{s_i} (chosen arbitrarily as 180° in this example). The position of $\{s_j\}$ relative to $\{s_i\}$ is denoted by $\vec{r}_{s_i s_j}$.

gathered from a model wave tank and full-scale experiments. The full-scale experiments involve a research vessel equipped with multiple IMUs and a commercial wave radar, operating in proximity to several wave buoys on the west coast of Norway. The wave estimation results show that our proposed method is competitive with existing wave measurement technology in terms of accuracy and online performance while costing a fraction, being portable, flexible, and robust against environmental impact.

2. Theory

2.1. Main idea

A pair of spatially distributed sensors in the water will generally experience a different delay than those on a rigid body. On the ocean surface, the sensors are decoupled from each other, meaning that the delay between the wave elevation measurements is solely determined by the distance between the sensors and the propagation angle and speed of the waves passing through them (Fig. 1(a)). On a rigid body, however, the sensors are interrelated, meaning that as soon as the waves come in contact with the body, all sensor measurements will be affected simultaneously (Fig. 1(b)).

The differences between the sensor delays in the aforementioned situations can be shown quantitatively through some simple kinematics. Consider the situation in Fig. 1(a) but from a bird's-eye view later in time as illustrated in Fig. 2. The delay between the measurements in sensor $\{s_j\}$ and $\{s_i\}$ manifests itself as either a phase, time, or path

difference (PTPD). The path difference d_{ij} is simply the distance along the wave propagation direction the wave must travel to get from $\{s_j\}$ to $\{s_i\}$. We obtain an expression for d_{ij} by decomposing the position vector $\vec{r}_{s_i s_j}$ in the wave tangent frame $\{w\}$, and extracting the resulting x-component. This operation is represented mathematically by

$$\mathbf{r}^w_{s_i s_j} = \mathbf{R}^w_{s_i} \mathbf{r}^{s_i}_{s_i s_j}, \tag{1}$$

where $\mathbf{r}^{s_i}_{s_i s_j} = [x_{ij}, y_{ij}, z_{ij}]^\top$ denotes the coordinate position vector of sensor $\{s_j\}$ relative to $\{s_i\}$ expressed in the sensor frame $\{s_i\}$ and $\mathbf{R}^w_{s_i}$ is a rotational transform between $\{s_i\}$ and $\{w\}$ given by

$$\mathbf{R}^w_{s_i} = \begin{bmatrix} \cos\beta & \sin\beta & 0 \\ \sin\beta & -\cos\beta & 0 \\ 0 & 0 & -1 \end{bmatrix}.$$

Carrying out the multiplication in Eq. (1) with the rotation matrix above, yields $\mathbf{r}^w_{s_i s_j} = [x_{ij}\cos\beta + y_{ij}\sin\beta, *, *]^\top$, where we have omitted the y and z components as they are not relevant. Hence, the path difference, which is the x-component of $\mathbf{r}^w_{s_i s_j}$, becomes $d_{ij} = x_{ij}\cos\beta + y_{ij}\sin\beta$, and the time it takes the wave to complete d_{ij} is simply

$$t_{ij} = \frac{d_{ij}}{c} = \frac{x_{ij}\cos\beta + y_{ij}\sin\beta}{c}, \tag{2}$$

where t_{ij} is the time difference between the measurements in $\{s_j\}$ and $\{s_i\}$, and c is the *wave celerity* or phase velocity, as it is also called. For a regular harmonic wave, the wave celerity is given by

$$c = \frac{\omega}{k}, \tag{3}$$

where ω and k denote the angular wave frequency and wave number, respectively. Substituting Eq. (3) into Eq. (2), yields

$$\Theta_{ij} = k(x_{ij}\cos\beta + y_{ij}\sin\beta), \tag{4}$$

where $\Theta_{ij} := \omega t_{ij}$ is the phase difference between the measurements in sensors $\{s_j\}$ and $\{s_i\}$.

Unfortunately, it is not straightforward to find a similar expression as Eq. (4) for the situation where the sensors are mounted on a rigid body (Fig. 1(b)). If the sensor output is evaluated as acceleration, the difference in acceleration between two arbitrary points (here labeled as s_j and s_i) on the rigid body is modeled by

$$\vec{a}_{ns_j} - \vec{a}_{ns_i} = \dot{\vec{\omega}}_{nb} \times \vec{r}_{s_i s_j} + \vec{\omega}_{nb} \times (\vec{\omega}_{nb} \times \vec{r}_{s_i s_j}), \tag{5}$$

where $\vec{a}_{ns_j}$ and $\vec{a}_{ns_i}$ are the accelerations of $\{s_j\}$ and $\{s_i\}$ relative to the navigational frame $\{n\}$,[1] $\vec{\omega}_{nb}$ represent the angular rates of the body frame $\{b\}$ relative to $\{n\}$, $\dot{\vec{\omega}}_{nb}$ is the angular acceleration, and $\vec{r}_{s_i s_j}$ is the position vector of $\{s_j\}$ relative to $\{s_i\}$. It is interesting to see from Eq. (5) that if the body simply oscillates up and down without any angular displacement (i.e., $\dot{\vec{\omega}}_{nb} = \vec{\omega}_{nb} = \vec{0}$), the accelerations in both sensors will be identical (i.e., zero delay). Hence, the measurement

---

[1] The navigational or North-East-Down frame $\{n\}$ is a local tangent frame with origin defined at the center of gravity of the navigated object and coordinates associated with Earth's reference ellipsoid. We consider the navigational frame to be Earth-fixed, which, for low-speed applications such as marine craft, enables $\{n\}$ to be approximated as an inertial frame of Ref. Fossen (2021).

delay perceived between sensors on a rigid body is caused by angular displacements about the body's roll, pitch, and yaw axes.

Although the cause of the sensor delays in Figs. 1(a) and 1(b) are inherently different (one is caused by the time it takes the wave to transit between the sensors, while the other is governed by the angular rates of the body induced by waves), they both share a common parameter, namely, the sensor separation distance $\vec{r}_{s_i s_j}$. If we decompose Eq. (5) in $\{b\}$ and introduce the coordinate vectors $\boldsymbol{\omega}_{nb}^b = [p, q, r]^\top$, $\dot{\boldsymbol{\omega}}_{nb}^b = [\dot{p}, \dot{q}, \dot{r}]^\top$, and $\mathbf{r}_{s_i s_j}^b = [x_{ij}, y_{ij}, z_{ij}]^\top$, we can rewrite Eq. (5) in terms of the sensor separation as

$$a_{ns_j,z}^b - a_{ns_i,z}^b = (pr - \dot{q})x_{ij} + (\dot{p} - qr)y_{ij} + (q^2 - p^2)z_{ij}, \tag{6}$$

where we have only considered the z-components of the accelerations as these are most relevant. As can be seen by studying Eqs. (4) and (6), the sensor separation $\mathbf{r}_{s_i s_j}^b = [x_{ij}, y_{ij}, z_{ij}]^\top$ and difference in acceleration (manifested as a difference in amplitude and phase between the signals) are *linearly* proportional. Using this fact, it is possible to apply the PTPD model to the situation in Fig. 1(b) by making the sensor separation sufficiently small. In this way, the sensor delays will become small enough that the models (4) and (6) almost yield the same result, and we can use the former to model the phase difference between a pair of sensors on a rigid body.[2]

2.2. A phase-time-path-difference model for surface vessels with constant forward speed

An important limitation of Eq. (4) is that it is based on a stationary pair of sensors, meaning that the model can only be applied to stationary vessels. As we shall see, we can generalize the phase difference model to account for speed such that it may be applied to situations in which the vessel is either stationary or moving.

In the following model derivation, consider the situation shown in Fig. 3, which depicts an underway vessel with a pair of distributed sensors, oriented at an angle relative to some incoming long-crested harmonic waves. Recall from Section 2.1 that the PTPD model was derived by projecting the relative sensor positions onto the wave tangent frame $\{w\}$ and extracting the resulting x-component to get the path difference d_{ij}. To carry out this operation for sensors on a rigid body, the rotational transform must be modified to account for the vessel roll and pitch angles induced by the waves (when the vessel oscillates due to the waves passing through it, the path difference d_{ij} changes, see Fig. 3(b)). Hence, a kinematic expression for d_{ij} can be obtained by transforming the body-fixed position vector $\vec{r}_{s_i s_j}$ from $\{s_i\}$ to $\{w\}$ using the rotational transform $\mathbf{R}_{s_i}^w$ according to Eq. (1), where $\mathbf{r}_{s_i s_j}^{s_i} = [x_{ij}, y_{ij}, z_{ij}]^\top$ denotes the body-fixed sensor coordinates expressed in $\{s_i\}$ and $\mathbf{R}_{s_i}^w$ is now defined by two sequences of intermediate rotations based on the *zyx*-convention (Fossen, 2021), i.e.,

$$\mathbf{R}_{s_i}^w = \mathbf{R}_{z,\beta}\mathbf{R}_{x,180°}\mathbf{R}_{y,\theta}\mathbf{R}_{x,\phi} = \begin{bmatrix} c\beta c\theta & c\beta s\theta s\phi + s\beta c\phi & c\beta s\theta c\phi - s\beta s\phi \\ s\beta c\theta & s\beta s\theta s\phi - c\beta c\phi & s\beta s\theta c\phi + c\beta s\phi \\ s\theta & -c\theta s\phi & -c\theta c\phi \end{bmatrix}, \tag{7}$$

where $s \cdot = \sin(\cdot)$ and $c \cdot = \cos(\cdot)$. Inserting Eq. (7) into Eq. (1) and carrying out the multiplication, yields $\mathbf{r}_{s_i s_j}^w = [x_{ij}c\beta c\theta + y_{ij}(c\beta s\theta s\phi + s\beta c\phi) + z_{ij}(c\beta s\theta c\phi - s\beta s\phi), *, *]^\top$, where we have omitted the y and z components as they are not relevant. The path difference d_{ij} is simply

the x-component of $\mathbf{r}_{s_i s_j}^w$ and the time it takes a wave to complete the distance d_{ij} is given by

$$t_{ij} = \frac{d_{ij}}{u_r} = \frac{x_{ij}c\beta c\theta + y_{ij}(c\beta s\theta s\phi + s\beta c\phi) + z_{ij}(c\beta s\theta c\phi - s\beta s\phi)}{u_r}, \tag{8}$$

where t_{ij} and u_r denote the corresponding time difference and x-component of the relative velocity between the waves and the vessel, respectively. In general, the velocity of the waves relative to the vessel can be expressed in the wave tangent frame $\{w\}$ as

$$\mathbf{v}_{bw'}^w = \mathbf{v}_{nw'}^w - \mathbf{v}_{nb}^w = \mathbf{v}_{nw'}^w - \mathbf{R}_b^w \mathbf{v}_{nb}^b = [c - U\cos\beta\cos\theta, *, *]^\top, \tag{9}$$

where $\mathbf{v}_{nw'}^w = [c, 0, 0]^\top$ and $\mathbf{v}_{nb}^b = [U, 0, 0]^\top$, respectively, represent the wave $\{w'\}$ and vessel $\{b\}$ velocities relative to the Earth-fixed navigational frame $\{n\}$, represented by the wave celerity c and forward vessel speed U. The rotational transform $\mathbf{R}_b^w$ is identical to Eq. (7) since $\{b\}$ and $\{s_i\}$ are aligned (see Fig. 3). Substituting u_r in Eq. (8) with the first component of Eq. (9), yields the time difference

$$t_{ij} = \frac{x_{ij}c\beta c\theta + y_{ij}(c\beta s\theta s\phi + s\beta c\phi) + z_{ij}(c\beta s\theta c\phi - s\beta s\phi)}{c - Uc\beta c\theta}. \tag{10}$$

The time difference can be converted to a phase difference Θ_{ij} by inserting Eq. (3) into Eq. (10), which gives

$$\Theta_{ij} = k(x_{ij}c\beta c\theta + y_{ij}(c\beta s\theta s\phi + s\beta c\phi) + z_{ij}(c\beta s\theta c\phi - s\beta s\phi)), \tag{11}$$

where $\Theta_{ij} := (\omega - kU\cos\beta\cos\theta)t_{ij}$. For well balanced vessels, the roll and pitch angles will on average be close to zero, i.e., $\bar{\phi} \equiv \mathbb{E}[\phi(t)] \approx 0$ and $\bar{\theta} \equiv \mathbb{E}[\theta(t)] \approx 0$, where $\mathbb{E}[\cdot]$ denotes the expected value. Based on this notion, we can derive the mean phase difference $\bar{\Theta}_{ij}$ by inserting the values $\bar{\phi} = 0$ and $\bar{\theta} = 0$ into Eq. (11), which yields

$$\bar{\Theta}_{ij} = k(x_{ij}\cos\beta + y_{ij}\sin\beta), \tag{12}$$

where the mean phase difference $\bar{\Theta}_{ij} := \omega_e t_{ij}$ is now defined in terms of the wave encounter frequency $\omega_e = \omega - kU\cos\beta$. By focusing on the average phase difference, we have conveniently circumvented the restrictive small-angle assumption considered in Dirdal et al. (2022). A quantitative assessment of the error impact due to the transition from Eq. (11) to Eq. (12) is given in Appendix. In the remainder of this study, we consider the phase difference as the principal sensor delay, as this quantity is most commonly treated in the literature.

2.3. Forward speed state-space model

The phase difference model (12) can be formulated into a state-space model by introducing the state vector $\mathbf{x} = [x_1, x_2]^\top = [\beta, k]^\top$ and polar coordinates ($x_{ij} = R_{ij}\cos\alpha_{ij}$, $y_{ij} = R_{ij}\sin\alpha_{ij}$), and rewriting Eq. (12) into the vector form

$$\bar{\Theta}_{ij} = \begin{bmatrix} R_{ij}\cos\alpha_{ij} & R_{ij}\sin\alpha_{ij} \end{bmatrix} \begin{bmatrix} x_2\cos x_1 \\ x_2\sin x_1 \end{bmatrix}.$$

For $N \geq 3$ number of sensors, the continuous-time state-space model can be written compactly as

$$\dot{\mathbf{x}} = \mathbf{0},$$

$$\mathbf{z} = \mathbf{h}(\mathbf{x}) = \underbrace{\begin{bmatrix} R_{12}\cos\alpha_{12} & R_{12}\sin\alpha_{12} \\ R_{13}\cos\alpha_{13} & R_{13}\sin\alpha_{13} \\ \vdots & \vdots \\ R_{1N}\cos\alpha_{1N} & R_{1N}\sin\alpha_{1N} \\ R_{23}\cos\alpha_{23} & R_{23}\sin\alpha_{23} \\ \vdots & \vdots \\ R_{2N}\cos\alpha_{2N} & R_{2N}\sin\alpha_{2N} \\ \vdots & \vdots \\ R_{(N-1)N}\cos\alpha_{(N-1)N} & R_{(N-1)N}\sin\alpha_{(N-1)N} \end{bmatrix}}_{\text{sensor configuration matrix}} \begin{bmatrix} x_2\cos x_1 \\ x_2\sin x_1 \end{bmatrix},$$

---

[2] For sensors on a rigid body, the sensor separation and phase difference are only proportional in a limited distance range. When the sensor separation grows to infinity, the phase difference will converge to $\pm 180°$, at which point the sensor measurements will be anti-phase.

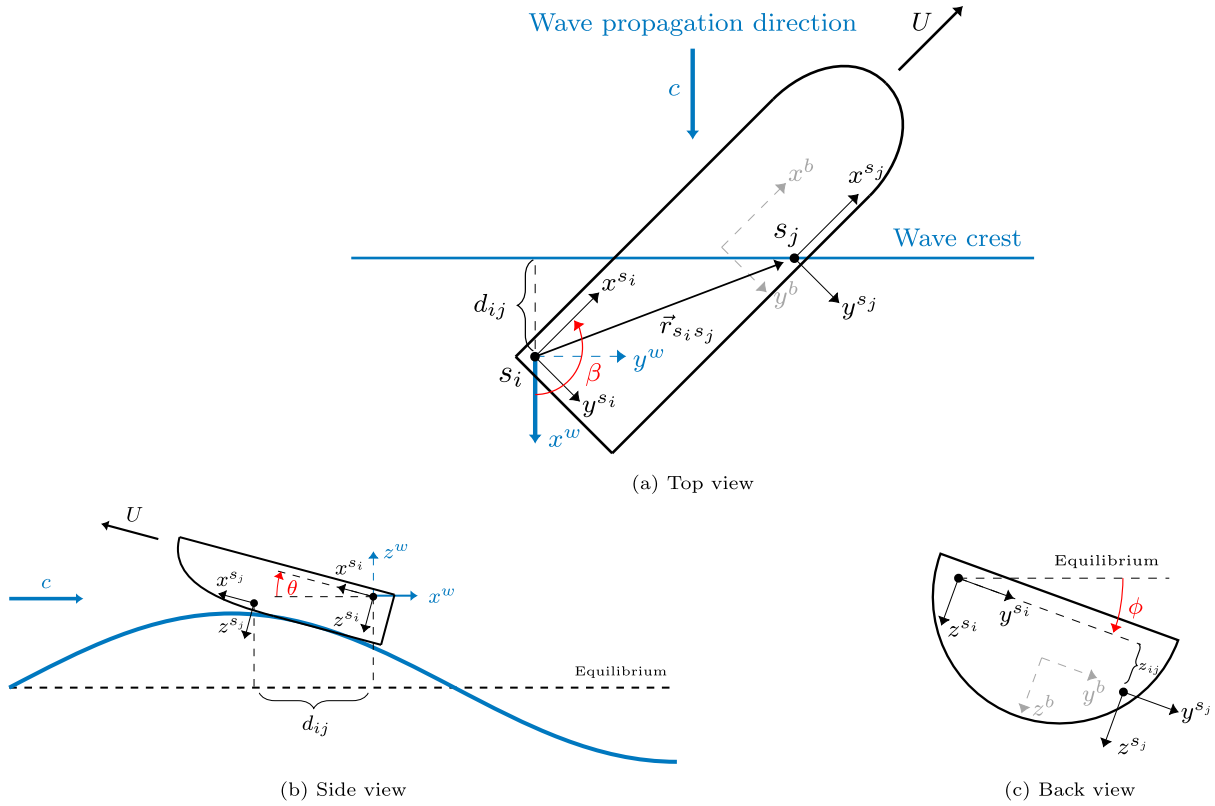$$\tag{13}$$

Fig. 3. Three independent situations of an underway vessel (rigid body) with constant forward speed U equipped with two sensors $\{s_i\}$ and $\{s_j\}$, oriented at an angle β relative to incoming long-crested harmonic waves with propagation speed c. The position of $\{s_j\}$ relative to $\{s_i\}$ is represented by $\vec{r}_{s_i s_j}$. The sensor axes point in the same direction as the vessel body frame $\{b\}$ (slightly faded). The tangent wave frame $\{w\}$ is attached to the vessel with axes (x^w, y^w, z^w) and origin coinciding with the (arbitrarily chosen) reference sensor $\{s_i\}$. The x^w axis points in the same direction as the propagating waves, z^w points upwards, and y^w completes the right-handed coordinate system. The distance the wave must travel to get from sensor $\{s_j\}$ to $\{s_i\}$ along the wave propagation direction is denoted d_{ij} and depends on the roll (ϕ), pitch (θ), and relative wave encounter (β) angles. The wave encounter angle β is defined as the angle from x^w to the projection of x^{s_i} onto the tangent plane $\{w\}$. Starboard incident waves are defined by $\beta \in (-180, 0]°$, whereas port incident waves are defined by $\beta \in (0, 180]°$. When $\beta = 0°$, the waves hit the stern first and we have following sea.

where $\mathbf{z} = [\bar{\Theta}_{12}, \ \bar{\Theta}_{13}, \ \ldots, \ \bar{\Theta}_{1N}, \ \bar{\Theta}_{23}, \ \ldots, \bar{\Theta}_{2N}, \ \ldots, \bar{\Theta}_{(N-1)N}]^\top$. The dimension of $\mathbf{z}$ is $P_N \times 1$, where P_N is the maximum number of independent phase difference measurements associated with N, which, for nonlinear arrays, can be computed from

$$P_N = \frac{N(N-1)}{2}. \tag{14}$$

The state-space model (13) is observable for a minimum of two independent phase differences, i.e., three noncollinear sensors (see Dirdal et al. (2022) for proof). As we shall see, if the sensor is an IMU, it is sufficient to only consider a *single* IMU and use the rigid-body measurement transform (5) to generate the remaining measurements needed in Eq. (13) to uniquely resolve the wave encounter angle and wave number. It is worth emphasizing that the state-space model (13) is observable in shallow and deep waters as it only utilizes the general equation for wave celerity (phase velocity) in its derivation. Hence, the PTPD approach is valid for all water depths, provided that the vessel undergoes sufficient wave excitation.

2.4. High-frequency waves

The wave undulations on the sea surface will trigger a heave response from the vessel as they move through it. If the waves are sufficiently long, the heave response will be similar to the wave elevation, except scaled in amplitude. However, if the waves are very short, the heave response will be dissimilar from the waves due to the effect of vessel lowpass filtering (Nielsen, 2007, 2008; de Souza et al., 2018; Nielsen et al., 2019; Nielsen and Dietz, 2020; Dirdal et al., 2022). The effect of vessel filtering occurs whenever the wavelength of a particular wave is shorter than the projected wave trajectory distance

through the vessel (Dirdal et al., 2022). When this happens, multiple wave crests will affect the vessel simultaneously, resulting in a distorted heave response. Hence, in order to avoid the effect of filtering, the wavelength λ should exceed the wave trajectory distance for a given wave direction β, i.e.,

$$\lambda > L|\cos\beta| + B|\sin\beta|, \tag{15}$$

where L and B represent the respective length and beam dimensions of the vessel. A quick and easy way to assess whether (15) holds for all β is to check if the given wavelength is larger than the diagonal length of the vessel (the maximum wave trajectory distance), i.e.,

$$\lambda > \sqrt{L^2 + B^2}. \tag{16}$$

If Eq. (16) holds, the effect of vessel filtering is avoided for all β and the vessel heave response will resemble the wave elevation (in other words, the vessel behaves like a buoy).

It is worth emphasizing that the effect of vessel filtering on sensor measurements is not accounted for by the PTPD model. As discussed in Section 2.1, the PTPD model merely uses the travel distance, propagation angle, and speed of the waves to quantify sensor delays and neglects any rigid body effects. It is, therefore, important to exercise caution when applying Eq. (13) to model the delay between shipboard sensors, especially if filtering is occurring. As we shall see in Section 3.3.3, this potential issue can be circumvented by employing criterion (16) in the estimation procedure.

2.5. Theoretical results

To summarize, a pair of sensors on the sea surface generally experience a different delay than those on a rigid body. However, the
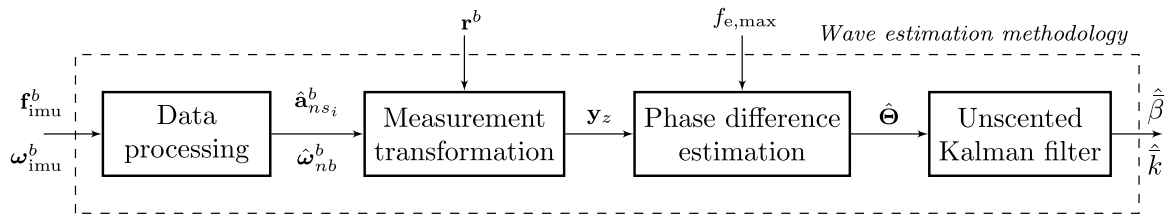
Fig. 4. A block diagram illustrating the four procedures involved in our wave estimation methodology. The input data comprises the specific force, $\mathbf{f}^b_{\mathrm{imu}}$, and angular rates, $\boldsymbol{\omega}^b_{\mathrm{imu}}$, from a shipboard IMU expressed in the vessel body frame $\{b\}$. The input data is processed to yield estimates of the linear acceleration, $\hat{\mathbf{a}}^b_{ns_i}$, and angular velocity, $\hat{\boldsymbol{\omega}}^b_{nb}$, which are then transformed to other locations on the vessel based on the desired lever arms $\mathbf{r}^b$. The z-components of the transformed accelerations are grouped into an acceleration matrix $\mathbf{y}_z$ and the phase differences $\hat{\boldsymbol{\Theta}}$ between them are estimated based on the frequency bandwidth $f_{\mathrm{e,max}}$. Finally, the phase differences are supplied to an unscented Kalman filter which yields estimates of the wave encounter angle $\hat{\beta}$ and wave number $\hat{k}$.

delays in both situations are proportional to the sensor separation up to a certain distance, although with different gradients. We conjecture that the forward speed PTPD model, which is simple, explicit, and observable in terms of the wave propagation direction and wave number, can be used to model the sensor delays on a rigid body given that the sensor separation distances are sufficiently small, and the waves are sufficiently long. These speculations can be compactly formulated into the following assumption:

Assumption 1. If Eq. (15) holds for a given λ and β and the separation distance between a pair of sensors on a rigid body is sufficiently small, then the state-space model (13) can accurately model the phase difference between the heave measurements in each sensor.

If Assumption 1 holds, then we are guaranteed by the observability proof of our state-space model that the relative wave propagation direction and wave number can be uniquely determined from phase differences between a group of sensors on a surface vessel (rigid body), which leads to the following theorem:

Theorem 1. *Consider a rigid body with constant forward speed $U \geq 0$, oriented at an angle β relative to the propagation direction of a regular wave (Fig. 3) with wave number k. If Assumption 1 holds, then β and k can be uniquely resolved from a minimum of three noncollinear sensors measuring the body's heave displacement or heave acceleration.*

Proof. See Dirdal et al. (2022).

It is worth mentioning that the vessel roll and pitch motion cannot be utilized with the PTPD approach as these motions do not exhibit any phase difference across various points on the body (recall that for a rigid body, angular motions are uniform for all points).

Suppose the sensors comprise a tri-axial accelerometer and gyroscope, such as an IMU. In that case, the minimum sensor requirements imposed by Theorem 1 can be relaxed to a single sensor by employing the acceleration transformation (5) to generate the other accelerations needed. This interesting result can be formulated into the following corollary:

Corollary 1.1. *If the sensor is an inertial measurement unit (IMU), then β and k can be uniquely resolved from a single IMU.*

Before we can assess the validity of these theoretical claims experimentally, we need to develop a methodology that enables us to transform the IMU measurements to different ship locations, extract the phase differences between the various measurements, and resolve the wave direction and wave number from the phase differences.

3. Methodology

Experimental verification of the theoretical results presented in Section 2.5 poses two crucial questions, namely, how to measure the phase difference between a pair of sensors and how to estimate

the wave direction and wave number from the phase differences. In this section, we address these questions by proposing a methodology (Fig. 4) for estimating the desired wave quantities. As we shall see, our methodology comprises a sequence of procedures, each of which will be discussed in the following subsections.

3.1. Data processing

The data processing steps performed on the raw IMU data involve data segmentation, DC-removal, and lowpass filtering. These steps are necessary to preserve the time-localization of events and clean the data by mitigating unwanted biases and high-frequency noise.

3.1.1. Data segmentation

The ocean surface behavior is a non-stationary process, which implies that its statistical parameters, such as wave height, direction, and frequency, are time-varying. It is paramount to account for this time variability when computing these parameters to correctly assess the present ocean state. For instance, if we consider a very long data time series and apply an FFT to this data, it becomes difficult to associate which peak frequencies (and consequently which wave directions) correspond to the actual time instances in which the events took place. Hence, to preserve the time-localization of events using an FFT, it is necessary to divide the data series into (quasi-stationary) segments and process each data segment individually. This strategy is applied to the input IMU data in the estimation procedure (Fig. 4).

The specific force and angular velocity data are segmented by multiplying the developing time series with a (moving) Hanning window of a predefined length. The Hanning window alleviates the effect of spectral leakage by smoothly decreasing the input to zero near the endpoints, reducing potential discontinuities between the first and final data samples. However, since the lower and upper tails of the Hanning window are close to zero, a significant portion of the time series will effectively be ignored in the analysis. To ensure that all information is considered in the analysis, we use a 50% overlap between subsequent segments, which is common for Hanning windows.

When segmenting the data for FFT analysis, a compromise ultimately arises between the time and frequency resolution of the resulting periodograms. The compromise between time and frequency is regulated by the length of the window function considered (a long window generally implies good frequency resolution but uncertainty in the time resolution, and vice versa). An upper bound for the window length can be established if the time intervals where the waveforms are quasi-stationary are known. For ocean waves, stationarity is generally preserved for up to 15–30 min (Holthuijsen, 2007).

3.1.2. DC removal and lowpass filtering

In general, the IMU measurements are subject to several stochastic errors, which are typically separated and modeled as additive zero-mean Gaussian white noise and a time-varying bias term. Adhering to

this approach, we can use the standard three-axis accelerometer and gyroscope sensor models from Fossen (2021), which are given as

$$\mathbf{f}^b_{\text{imu}} = \mathbf{a}^b_{ns_i} - \mathbf{g}^b + \mathbf{b}^b_{\text{acc}} + \mathbf{w}^b_{\text{acc}},$$
$$\boldsymbol{\omega}^b_{\text{imu}} = \boldsymbol{\omega}^b_{nb} + \mathbf{b}^b_{\text{ars}} + \mathbf{w}^b_{\text{ars}}, \tag{17}$$

where $\mathbf{f}^b_{\text{imu}}$ and $\boldsymbol{\omega}^b_{\text{imu}}$ are the respective specific force and angular velocity measurements, $\mathbf{a}^b_{ns_i}$ and $\boldsymbol{\omega}^b_{nb}$ are the linear acceleration and angular velocity of the sensor frame $\{s_i\}$ with respect to $\{n\}$ (considered Earth-fixed and assumed inertial), $\mathbf{b}^b_{\text{acc}}$ and $\mathbf{b}^b_{\text{ars}}$ denote the respective sensor biases, $\mathbf{w}^b_{\text{acc}}$ and $\mathbf{w}^b_{\text{ars}}$ denote the respective sensor noises, and $\mathbf{g}^b$ denotes the gravitational acceleration. All quantities are expressed in $\{b\}$.

As can be seen by studying Eq. (17), the IMU measurements are generally centered around a non-zero value due to the sensor biases and force of gravity. If left unaccounted for, this non-zero value or DC-offset will show up in the first frequency bin of the FFT spectrum and may leak power into adjacent bins, affecting other low-frequency components. Hence, it is advantageous to remove the DC-offset before FFT processing. The latter can be achieved by simply averaging each measurement time series and subtracting the average from itself. In order to reduce the effect of high-frequency noise on the average and the angular velocity (which shall be differentiated later), we apply a lowpass filter with a cut-off frequency above the bandwidth of the considered waves (for how to select this cut-off frequency, see Section 3.3.3) to the IMU measurement segment. Hence, the final estimated acceleration and angular velocity segments are given by

$$\hat{\mathbf{a}}^b_{ns_i} = \bar{\mathbf{f}}^b_{\text{imu}} - \mathbb{E}[\bar{\mathbf{f}}^b_{\text{imu}}],$$
$$\hat{\boldsymbol{\omega}}^b_{nb} = \bar{\boldsymbol{\omega}}^b_{\text{imu}} - \mathbb{E}[\bar{\boldsymbol{\omega}}^b_{\text{imu}}], \tag{18}$$

where $\bar{\mathbf{f}}^b_{\text{imu}}$ and $\bar{\boldsymbol{\omega}}^b_{\text{imu}}$ are the lowpass filtered signals and $\mathbb{E}[\cdot]$ denotes the expected value. The averaging operation in Eq. (18) tacitly assumes that the accelerometer and gyroscope biases in Eq. (17) remain more or less constant for the duration of each considered data segment. The validity of this assumption can be assessed by evaluating the accelerometer and gyroscope in-run bias stabilities found in the IMU datasheet for the time duration of the data segments. We assess the bias stability for the IMUs considered in the wave tank and full-scale experiments in Sections 4.1.3 and 5.1.2, respectively.

3.2. Measurement transformation

The acceleration at one specific point on a rigid body can be transformed to any other location, provided that the body's angular velocity and angular acceleration are known. This measurement transformation is given in Eq. (5) and can be decomposed in the body frame $\{b\}$ as follows

$$\mathbf{a}^b_{ns_j} = \mathbf{a}^b_{ns_i} + \dot{\boldsymbol{\omega}}^b_{nb} \times \mathbf{r}^b_{s_i s_j} + \boldsymbol{\omega}^b_{nb} \times (\boldsymbol{\omega}^b_{nb} \times \mathbf{r}^b_{s_i s_j}), \tag{19}$$

where $\mathbf{a}^b_{ns_j}$ is the transformed linear acceleration of virtual sensor $\{s_j\}$, $\mathbf{a}^b_{ns_i}$ is the physical linear acceleration of sensor $\{s_i\}$, $\dot{\boldsymbol{\omega}}^b_{nb}$ is the angular acceleration, and $\mathbf{r}^b_{s_i s_j}$ is the position of $\{s_j\}$ relative to $\{s_i\}$. If we replace $\mathbf{a}^b_{ns_i}$ and $\boldsymbol{\omega}^b_{nb}$ in Eq. (19) with our estimated quantities $\hat{\mathbf{a}}^b_{ns_i}$ and $\hat{\boldsymbol{\omega}}^b_{nb}$ from Section 3.1.2, we can use Eq. (19) to generate any virtual measurements needed by supplying the desired lever arms (sensor separation distances) $\mathbf{r}^b_{s_i s_j}$. The main challenge with this approach, however, is that it requires an accurate estimate of $\dot{\boldsymbol{\omega}}^b_{nb}$, which is not usually measured. In this study, we obtain estimates of the latter quantity by numerically differentiating $\hat{\boldsymbol{\omega}}^b_{nb}$. The data processing steps addressed in Section 3.1.2 ensure that the noise in $\hat{\boldsymbol{\omega}}^b_{nb}$ will not be significantly amplified by differentiation. After the desired amount of virtual accelerations have been generated, we extract the z-components of all of them and place them into an acceleration matrix $\mathbf{y}_z \in \mathbb{R}^{N \times L}$, consisting of N z-accelerations of length L.

Algorithm 1 Phase difference estimation

procedure PD($\mathbf{y}_z$, $f_{\text{e,max}}$)

  $\hat{\mathbf{Y}}_z \leftarrow \text{fft}(\mathbf{y}_z)$ ▷ Compute the FFT

  $\hat{\boldsymbol{\Theta}}_z \leftarrow \text{atan2}\left(\text{imag}(\hat{\mathbf{Y}}_z), \text{real}(\hat{\mathbf{Y}}_z)\right)$ ▷ Compute the phase response

  $\mathbf{f}_p \leftarrow \max_{0 \le f \le f_{\text{e,max}}} |\hat{\mathbf{Y}}_z|$ ▷ Store the peak frequencies (within $f_{\text{e,max}}$) in a vector

  for f in $\mathbf{f}_p$ **do**

    $[\hat{\Theta}_1, \hat{\Theta}_2, \ldots, \hat{\Theta}_N]^\top \leftarrow \hat{\boldsymbol{\Theta}}_z(f)$ ▷ Extract the phase values at frequency f

    $\hat{\Theta}_{ij} = \hat{\Theta}_i - \hat{\Theta}_j, \quad 1 \le i \le N-1,\ 2 \le j \le N,\ i < j$ ▷ Compute the phase differences for all i and j

    $\hat{\boldsymbol{\Theta}}(k) \leftarrow [\hat{\Theta}_{12}, \hat{\Theta}_{13}, \ldots, \hat{\Theta}_{(N-1)N}]^\top$ ▷ Store the phase differences for each f in a matrix

    $k \leftarrow k + 1$

  end for

  return $\hat{\boldsymbol{\Theta}}$

end procedure

3.3. Phase difference estimation

We estimate the phase differences between the measured waveforms by employing an FFT with a frequency threshold to avoid wave components potentially distorted by the vessel in question. The estimation procedure is shown in Algorithm 1 and compromises the following sequence of steps:

1. Compute the FFTs and phase responses of $\mathbf{y}_z$.
2. Find the peak frequency of each magnitude response within a maximum frequency threshold $f_{\text{e,max}}$.
3. Extract the phase values for each peak frequency.
4. Compute the phase differences.

In this procedure, it is tacitly assumed that the dominant frequency of the forced oscillation in heave aligns with the frequency of the external wave force. This assumption is generally valid when the ship encounters a fully developed sea with sufficiently large wave amplitude and wavelength (see Assumption 1). In the following subsections, we elaborate on additional implementation details not mentioned in Algorithm 1.

3.3.1. Zero padding

The input to Algorithm 1 is the acceleration matrix $\mathbf{y}_z \in \mathbb{R}^{N \times L}$. If L is a power of two, radix-2 FFT algorithms can be used to compute the frequency responses, which are very efficient and can reduce processing time. If L is not a power of two, radix-2 FFT algorithms may still be applied by appending zeros at the end of the time domain signals such that the total signal length becomes a power of two.

3.3.2. Tolerance threshold

The inverse tangent function used to obtain the phase response in Algorithm 1 is highly susceptible to rounding errors. As a result, the

rounding errors typically appear as noisy spikes in the computed phase response. A common strategy used to mitigate this problem is to define a tolerance threshold ϵ and zero out the values of $\hat{\mathbf{Y}}_z$ for which $|\hat{\mathbf{Y}}_z| < \epsilon$.

3.3.3. Frequency threshold

As discussed in Section 2.4, the vessel will distort wave components passing through it if the wavelengths are sufficiently short. In reality, an irregular sea comprises multiple wave components, some of which have wavelengths shorter than the wave trajectory distance through the vessel. It is, therefore, essential to avoid such wave components when processing the heave response. The latter can be achieved by only considering the frequency components within the upper threshold $f_{e,\max}$ of the FFT spectrum. Apart from scaling, sinusoidal components within this range are deemed unaffected by the vessel.

For stationkeeping vessels (i.e., $U = 0$), the zero-speed upper threshold $f_{\max}$ is the frequency in which the right hand side (RHS) and left hand side (LHS) of Eq. (15) become equal, which occurs when

$$f_{\max} = \sqrt{\frac{g/2\pi}{\sqrt{L^2 + B^2}} \tanh\left(\frac{2\pi d}{\sqrt{L^2 + B^2}}\right)}, \tag{20}$$

where g is the gravitational constant and d is the water depth. The relationship above is derived by rewriting Eq. (15) in terms of the wave number (i.e., $k = 2\pi/\lambda$), and inserting the resulting expression for k into the dispersion relation

$$\omega^2 = kg \tanh(kd). \tag{21}$$

For underway vessels (i.e., $U > 0$), the frequency threshold (20) needs to be adjusted to account for the Doppler shift given by

$$\omega_e = |\omega - kU \cos \beta|, \tag{22}$$

where ω_e is the Doppler shifted encounter frequency. Rewriting Eq. (22) in terms of linear frequency and $f_{\max}$, yields the adjusted maximum frequency threshold $f_{e,\max}$ given in terms of forward speed, i.e.,

$$f_{e,\max} = \left| f_{\max} \pm \frac{UL}{L^2 + B^2} \right|, \tag{23}$$

where we have used $k = 2\pi/\sqrt{L^2 + B^2}$ and $\cos \beta = \pm L/\sqrt{L^2 + B^2}$ (worst case scenario in which the wave trajectory distance is maximum). The latter component on the RHS of (23) should be added or subtracted depending on whether the vessel is following or moving against the waves, respectively.

3.4. Unscented Kalman filter

The state-space model (13) is inherently nonlinear, which requires nonlinear estimation techniques to resolve the desired wave quantities. Although it is possible to solve the wave direction analytically from Eq. (12), the Kalman filter framework offers several benefits over such an approach. With the Kalman filter, it is easy to incorporate uncertainties into the estimation procedure, handle multiple measurements, and simultaneously estimate the wave direction and wave number online (Dirdal et al., 2022). It is, however, necessary for the wave number to be positive, posing a constraint on the state estimate.

As discussed in Dirdal et al. (2022), the unscented Kalman filter (UKF) has certain advantages over the extended Kalman filter (EKF) when constraints are imposed on the state estimates. In short, the UKF accounts for constraints when updating the error covariance, which the EKF ultimately neglects. For this reason, the UKF was selected as our main algorithm and the following subsections explain how it may be applied to yield the desired wave quantities.

3.4.1. Algorithm

The UKF algorithm may be applied to discrete-time nonlinear dynamical systems of the form

$$\begin{aligned} \mathbf{x}_k &= \mathbf{f}(\mathbf{x}_{k-1}) + \mathbf{w}_k, \quad \mathbf{w}_k \sim \mathcal{N}(\mathbf{0}, \mathbf{Q}) \\ \mathbf{z}_k &= \mathbf{h}(\mathbf{x}_k) + \mathbf{v}_k, \quad \mathbf{v}_k \sim \mathcal{N}(\mathbf{0}, \mathbf{R}) \end{aligned} \tag{24}$$

where $\mathbf{x}_k := \mathbf{x}(kT_s)$ and $\mathbf{z}_k := \mathbf{z}(kT_s)$ constitute the sampled state and measurement vectors for sample time T_s and number k (not to be confused with the wave number), $\mathbf{f}$ and $\mathbf{h}$ represent nonlinear transition functions, and $\mathbf{w}_k$ and $\mathbf{v}_k$ denote white Gaussian process and measurement noise with covariance $\mathbf{Q}$ and $\mathbf{R}$, respectively. If we discretize the continuous-time state-space model (13) and compare it with Eq. (24), it is clear that the former fits the required model form with $\mathbf{f}(\mathbf{x}_{k-1}) = \mathbf{x}_{k-1}$ and $\mathbf{h}(\mathbf{x}_k)$ as before. The process and measurement noise $\mathbf{w}_k$ and $\mathbf{v}_k$ represent the expected deviation between reality and our process and measurement models. They are characterized statistically through their covariance matrices $\mathbf{Q}$ and $\mathbf{R}$, which are discussed in detail in Sections 3.4.2 and 3.4.3, respectively.

The UKF algorithm with state constraints is given in Algorithm 2; for relevant background material regarding the UKF and constraint handling, the reader is referred to Brown and Hwang (1997), Julier and Uhlmann (2004), Kandepu et al. (2008), and Simon (2010) and references therein. As a general rule, the UKF uses a deterministic sampling scheme to select its sigma points. In this paper, we have chosen the following set of sigma points

$$X_k^{(i)} = \begin{cases} \hat{\mathbf{x}}_k^-, & i = 0 \\ \hat{\mathbf{x}}_k^- + \sqrt{(M + \lambda)\hat{\mathbf{P}}_k^-}, & i = 1, \dots, M \\ \hat{\mathbf{x}}_k^- - \sqrt{(M + \lambda)\hat{\mathbf{P}}_k^-}, & i = M + 1, \dots, 2M \end{cases} \tag{25}$$

where

$\lambda = \alpha^2(L + \kappa) - M$

$M = \text{dimension of state } \mathbf{x}_k$

$\alpha = \text{spread of samples about the mean}$

$\kappa = \text{scaling factor}$

Sigma points outside the feasible region are projected onto the boundary using the projection

$$P(\hat{x}_2) = \begin{cases} \epsilon, & \hat{x}_2 < \epsilon \\ \hat{x}_2, & \text{otherwise} \end{cases} \tag{26}$$

where $\hat{x}_2$ is the wave number estimate and ϵ is a small positive number representing the boundary of the feasible region. The sigma points are then propagated through the nonlinear transform (13) to yield a new cloud of transformed points. The statistics of these points are then computed by weighting them together using the following sets of weights

$$W_\mu^{(0)} = \frac{\lambda}{\lambda + M}, \quad W_\mu^{(0 < i \le 2M)} = \frac{1}{2(\lambda + M)}, \tag{27}$$

$$W_\sigma^{(0)} = W_\mu^{(0)} + 1 - \alpha^2 + \gamma, \quad W_\sigma^{(0 < i \le 2M)} = \frac{1}{2(\lambda + M)}. \tag{28}$$

3.4.2. Process noise covariance

The conditions of the ocean environment, including wave direction and wave number, are generally time-varying. Assuming that the desired wave quantities are slowly varying, we can accommodate this variability by modifying the state-space model (13) to include white Gaussian noise with variance σ_w^2. The modified state-space model now becomes a Gaussian random walk process of the form

$$\dot{\mathbf{x}} = \mathbf{A}\mathbf{x} + \mathbf{G}\mathbf{w}, \quad \mathbf{w} \sim \mathcal{N}(\mathbf{0}, \mathbf{D}\delta(t - \tau)), \tag{29}$$

where $\mathbf{A} = \mathbf{0}_2$ (2×2 zero matrix), $\mathbf{G} = I_2$ (2×2 identity matrix), $\mathbf{D} = \sigma_w^2 I_2$, and $\delta(t - \tau)$ is the Dirac delta function. For simplicity, we

---

Algorithm 2 Unscented Kalman filter

---

procedure UKF($\hat{\mathbf{x}}_k^-, \hat{\mathbf{P}}_k^-, \mathbf{z}_k$)

     $X_k^{(i)} \leftarrow \text{Sigma}(\hat{\mathbf{x}}_k^-, \hat{\mathbf{P}}_k^-)$ ▷ Compute sigma points using Eq. (25)

     $X_c^{(i)} \leftarrow P(X_k^{(i)})$ ▷ Project sigma points using Eq. (26)

     $\hat{\mathbf{x}}_k^- \leftarrow \sum_{i=0}^{2M} W_\mu^{(i)} X_c^{(i)}$ ▷ Compute the apriori state estimate with Eq. (27)

     $\hat{\mathbf{P}}_k^- \leftarrow \left\{ \sum_{i=0}^{2M} W_\sigma^{(i)} (X_c^{(i)} - \hat{\mathbf{x}}_k^-)(X_c^{(i)} - \hat{\mathbf{x}}_k^-)^\top \right\} + \mathbf{Q}$ ▷ Compute the apriori error covariance with Eq. (28)

     $Z_k^{(i)} \leftarrow \mathbf{h}(X_c^{(i)})$ ▷ Propagation of sigma points using Eq. (13)

     $\hat{\mathbf{z}}_k^- \leftarrow \sum_{i=0}^{2M} W_\mu^{(i)} Z_k^{(i)}$ ▷ Predicted measurement

     $\hat{\mathbf{S}}_k \leftarrow \left\{ \sum_{i=0}^{2M} W_\sigma^{(i)} (Z_k^{(i)} - \hat{\mathbf{z}}_k^-)(Z_k^{(i)} - \hat{\mathbf{z}}_k^-)^\top \right\} + \mathbf{R}$ ▷ Compute the innovation covariance

     $\hat{\mathbf{P}}_k^{\mathbf{xz}} \leftarrow \sum_{i=0}^{2M} W_\sigma^{(i)} (X_c^{(i)} - \hat{\mathbf{x}}_k^-)(Z_k^{(i)} - \hat{\mathbf{z}}_k^-)^\top$ ▷ Compute the cross-covariance

     $\mathbf{K}_k \leftarrow \hat{\mathbf{P}}_k^{\mathbf{xz}} \hat{\mathbf{S}}_k^{-1}$ ▷ Compute the Kalman gain

     $\hat{\mathbf{x}}_k \leftarrow \hat{\mathbf{x}}_k^- + \mathbf{K}_k(\mathbf{z}_k - \hat{\mathbf{z}}_k^-)$ ▷ Compute posterior state estimate

     $\hat{\mathbf{P}}_k \leftarrow \hat{\mathbf{P}}_k^- - \mathbf{K}_k \hat{\mathbf{S}}_k \mathbf{K}_k^\top$ ▷ Compute posterior error covariance

     return $\hat{\mathbf{x}}_k, \hat{\mathbf{P}}_k$

end procedure

---

have used the same variance σ_w^2 to describe the variability of the wave direction and wave number. From basic control theory, it can be shown that the exact discretization of Eq. (29) is given by

$$\mathbf{x}_k = \mathbf{F}\mathbf{x}_{k-1} + \mathbf{w}_k,$$

where $\mathbf{F} = e^{T_s \mathbf{A}} = I_2$ and

$$\mathbf{w}_k = \int_{t_{k-1}}^{t_k} e^{(t_k - \tau)\mathbf{A}} \mathbf{G}\mathbf{w}(\tau)d\tau = \int_{t_{k-1}}^{t_k} \mathbf{w}(\tau)d\tau,$$

where we have simplified the latter expression by inserting the values for $\mathbf{A}$ and $\mathbf{G}$ into it. The process noise covariance $\mathbf{Q}$ is given by

$$\mathbf{Q} = \mathbb{E}[\mathbf{w}_k \mathbf{w}_k^\top] = T_s \mathbf{D} = T_s \sigma_w^2 I_2, \tag{30}$$

where $T_s = t_k - t_{k-1}$ denotes the sampling period.

3.4.3. Measurement noise covariance

Both the phase difference measurements $\mathbf{z}_k$ and measurement model $\mathbf{h}(\mathbf{x}_k)$ are subject to uncertainties that will cause discrepancies between them. The discrepancies are modeled by white Gaussian noise $\mathbf{v}_k$, which—if adequately designed (i.e., choosing the noise covariance $\mathbf{R}$ appropriately)—can account for prevalent errors. In this work, we deem errors caused by (i) submodeling and (ii) the FFT to be most fundamental to any deviations observed. It is important to address these errors to get an estimate of the uncertainties in the desired wave quantities, which, in turn, indicate whether they can be relied on or not.

The errors caused by (i) can be divided into two distinct groups: (a) errors due to the model simplification performed on Eq. (11) (i.e., averaging the instantaneous phase differences), and (b) errors resulting from the fact that we are applying a PTPD model to the phase differences on a rigid body. The phase difference error caused by (a) can be quantitatively assessed by evaluating the absolute difference between Eqs. (11) and (12), which, for an arbitrary pair of sensors, yields

$$|\Theta_{ij} - \bar{\Theta}_{ij}| = \Big| kR_{ij}\big(c\beta c\alpha_{ij}(c\theta - 1) + c\beta s\theta s\phi s\alpha_{ij} \\ + s\beta s\alpha_{ij}(c\phi - 1)\big) + kz_{ij}\big(c\beta s\theta c\phi - s\beta s\phi\big) \Big|. \tag{31}$$

In all the wave tank experiments, the model error (31) was less than 1° for all experimental wave parameters and sensor pairs (see Appendix). We deem errors of this magnitude minor and, as we shall see, are also dominated by the error incurred from (ii). For these reasons, we neglect errors due to (a) in the measurement covariance.

In contrast to (a), model deviations caused by (b) are considerably more challenging to quantify. The challenge arises because we lack a model quantifying directly how the phase changes when a measurement is transformed using Eq. (19) (if we had such an explicit model this would render the PTPD approach redundant). In order to assess the impact of (b), we rely on experimental data to quantify the deviation between the true phase differences and those predicted by our PTPD model. The experimental results from the wave tank show that the model error caused by (b) depends on the separation distance between the sensors. Hence, if the sensors are sufficiently close, (b) can safely be neglected from the measurement noise covariance without incurring significant errors. A discussion of the sensor separation is given in Section 4.2.1.

The phase difference error associated with (ii) can be attributed to spectral leakage, which occurs whenever the considered waveform is not periodic within the given sample interval. In other words, if the actual waveform frequency is not an integer multiple of the frequency resolution, the former will not be in the exact center of an FFT frequency bin, causing a spread of power into neighboring bins. For waveforms of finite duration comprising multiple frequencies, spectral leakage will generally persist as all the frequency components will generally not be integer multiples of the frequency resolution. An analysis of the FFT phase error resulting from spectral leakage is given by Dishan (1995), who shows that the error can be quantified as

$$\tilde{\Theta} = \pi T \tilde{f}, \tag{32}$$

where $\tilde{\Theta} := \hat{\Theta} - \Theta$ is the phase error between the true and estimated phase (represented by a hat), T is the duration of the considered waveform, and $\tilde{f} := \hat{f}_n - f$ is the frequency error between the true frequency and estimated frequency bin $\hat{f}_n = n/T$ for $n = 0, 1, \ldots, L/2-1$, where L denotes the transform length. The maximum frequency error occurs whenever the true frequency resides in the exact middle of two frequency bins, i.e.,

$$\tilde{f}_{\max} = \frac{\Delta}{2},$$

where $\Delta = 1/T$ is the frequency resolution. Inserting the latter into Eq. (32), yields the maximum phase error, i.e.,

$$\tilde{\Theta}_{\max} = \frac{\pi}{2}. \tag{33}$$

Based on Eq. (33), the upper error bound of the computed phase difference $\Theta_{ij} = \Theta_i - \Theta_j$ becomes

$$|\tilde{\Theta}_{ij}| = |\hat{\Theta}_{ij} - \Theta_{ij}| = |(\hat{\Theta}_i - \Theta_i) - (\hat{\Theta}_j - \Theta_j)| = |\tilde{\Theta}_i - \tilde{\Theta}_j| \leq |\tilde{\Theta}_i| + |\tilde{\Theta}_j| \leq \pi. \tag{34}$$

Although the theoretical error bound (34) is significant and may dissuade the FFT for phase estimation, in practice, we see that employing a Hanning window with the FFT leads to very accurate phase difference estimates by reducing spectral leakage.[3] Moreover, the main focus of this study is not optimality but rather a proof of concept of the PTPD approach to rigid bodies. As we shall see, the FFT algorithm is sufficient to achieve the latter goal.

The error bound (34) indicates that the true phase difference can be located *anywhere* within $\pm\pi$ of the estimated phase difference. This

---

[3] Multiple regular wave experiments were considered, and the phase difference estimates produced by the FFT with a Hanning window and curve fitting (considered ground truth) agreed very well.

Table 1
A summary of the initial state estimates, covariances, and internal parameters used in the UKF.

UKF initialization	$\hat{\mathbf{x}}_0 = [0, \ 0.05]^\top$
	$\hat{\mathbf{P}}_0 = \text{diag}([\frac{1}{3}\pi^2, \ 2])$
Process and measurement covariance	Wave tank experiments
	$\mathbf{Q} = T_s \sigma_w^2 I_2, \quad \sigma_w = 1 \times 10^{-3}$
	$\mathbf{R} = \frac{1}{3}\pi^2 I_{P_N}$
	Full-scale experiments
	$\mathbf{Q} = T_s \sigma_w^2 I_2, \quad \sigma_w = 1 \times 10^{-1}$
	$\mathbf{R} = \frac{1}{72}\pi^2 I_{P_N}$
UKF parameters	$M = 2, \quad \alpha = 0.01, \quad \gamma = 2, \quad \kappa = 0$

type of uncertainty is characteristic of a uniform distribution with zero mean and variance

$$\sigma^2_{\Theta_{\text{fft}}} = \frac{1}{3}\pi^2. \tag{35}$$

However, the UKF algorithm requires the measurement noise $\mathbf{v}_k$ to be zero mean Gaussian distributed. To accommodate this requirement, we approximate the uniform distribution above by a Gaussian with variance (35).

It is worth highlighting that there are no uncertainties in the virtual sensor locations when using the measurement transformation (19) to generate the virtual measurements. Hence, by employing Eq. (19) we eliminate uncertainties in the sensor locations as an error source, which were considered prominent in our previous work (Dirdal et al., 2022).

3.4.4. Initial parameter settings

A summary of the initialization parameters, process and measurement covariances, and internal parameters used in Algorithm 2 are listed in Table 1. It is worth stressing that faster convergence may be achieved by initializing the wave number to the value given by the dispersion relation (21) using the frequency obtained from the FFT. In this paper, however, we chose the initial values in Table 1 to demonstrate the validity of Theorem 1.

The initially estimated error covariance $\hat{\mathbf{P}}_0$ was selected by modeling the initial wave direction error as a uniform distribution over the interval $(-\pi, \pi]$ and approximating it by a Gaussian distribution with the same variance. The wave number variance was chosen heuristically but relatively large, reflecting our uncertainty in the actual value. The process and measurement covariance, $\mathbf{Q}$ and $\mathbf{R}$, were selected based on our analysis in Sections 3.4.2 and 3.4.3. Note that the sets of values for $\mathbf{Q}$ and $\mathbf{R}$ were chosen slightly differently in the wave tank and full-scale experiments to represent the conditions of the wave environment considered. For instance, in the wave tank, the wave conditions were completely stationary (represented by a low σ_w), whereas, in the ocean, the wave conditions were considerably more variable (represented by a larger σ_w). In the full scale experiments, the measurement covariance was reduced as this yielded better estimation results. As discussed in Section 3.4.3, we deem this reduction acceptable as the FFT phase estimates were generally very close to the ground truths in the wave tank experiments.

3.5. Summary of methodology

Our complete wave direction and wave number estimation methodology is given in Algorithm 3, merging all the procedures discussed in this section into one algorithm that is recursively applied for each new data segment. The input to Algorithm 3 comprises a data segment of the raw specific force and angular velocity measurements expressed in the vessel body frame $\{b\}$ from a single IMU, the desired (virtual) locations of the other IMU measurements (i.e., sensor separation distances), and a maximum frequency threshold $f_{\max}$ denoting the bandwidth of the

---

Algorithm 3 Wave direction and wave number estimation algorithm

procedure WDN($\mathbf{f}^b_{\text{imu}}$, $\boldsymbol{\omega}^b_{\text{imu}}$, $\mathbf{r}^b$, $f_{\max}$)

  $f_{\text{e,max}} \leftarrow \text{Doppler}(f_{\max})$ ▷ Compute the Doppler frequency threshold using (23) with vessel speed U

  $\hat{\mathbf{a}}^b_{ns_i}, \hat{\boldsymbol{\omega}}^b_{nb} \leftarrow \text{DP}(\mathbf{f}^b_{\text{imu}}, \boldsymbol{\omega}^b_{\text{imu}}, f_{\text{e,max}})$ ▷ Data processing using (18) with $f_{\text{e,max}}$ as cut-off frequency

  $\mathbf{y}_z \leftarrow \text{MT}(\hat{\mathbf{a}}^b_{ns_i}, \hat{\boldsymbol{\omega}}^b_{nb}, \mathbf{r}^b)$ ▷ Measurement transformation using (19) with virtual sensor locations $\mathbf{r}^b$

  $\hat{\boldsymbol{\Theta}} \leftarrow \text{PD}(\mathbf{y}_z, f_{\text{e,max}})$ ▷ Phase difference estimation given by Algorithm 1

  for $i = 1 : \text{length}(\hat{\boldsymbol{\Theta}})$ **do**

    $\hat{\mathbf{x}}, \hat{\mathbf{P}} \leftarrow \hat{\mathbf{x}}_0, \hat{\mathbf{P}}_0$ ▷ Initial state and covariance estimates given in Table 1

    for $j = 1 : \text{length}(\mathbf{y}_z)$ **do**

      $\mathbf{z} \leftarrow \hat{\boldsymbol{\Theta}}(i)$ ▷ Extract phase differences corresponding to each peak frequency

      $\hat{\mathbf{x}}, \hat{\mathbf{P}} \leftarrow \text{UKF}(\hat{\mathbf{x}}, \hat{\mathbf{P}}, \mathbf{z})$ ▷ Wave direction and number estimation given by Algorithm 2

    end for

    $\hat{\mathbf{X}}(i) \leftarrow \hat{\mathbf{x}}$ ▷ Store final wave estimate from UKF

  end for

  $\hat{\bar{\beta}}, \hat{\bar{k}} \leftarrow \text{mean}(\hat{\mathbf{X}})$ ▷ Extract average wave direction and wave number estimates

  return $\hat{\bar{\beta}}, \hat{\bar{k}}$

end procedure

---

considered waves. The frequency threshold should not exceed the upper threshold given by Eq. (20) and, if the vessel is moving with speed U, should be adjusted to $f_{\text{e,max}}$ by considering Eq. (23) (when $U = 0$, $f_{\text{e,max}}$ reduces to $f_{\max}$). The length of the considered data segment and percentage overlap with consecutive segments are generally tunable parameters. As we shall see, these parameters regulate the trade-off between accuracy and online estimation performance and should be carefully selected.

The estimated phase differences matrix $\hat{\boldsymbol{\Theta}}$ from Algorithm 1 has dimension $P_N \times N$, which means there are N sets of phase differences pertaining to each peak frequency. For this reason, the UKF algorithm must be applied N times to account for each, potentially different, set of phase differences, which, in turn, yields N separate wave estimates. We take the average of all these estimates and report this as the final estimated wave direction and wave number.
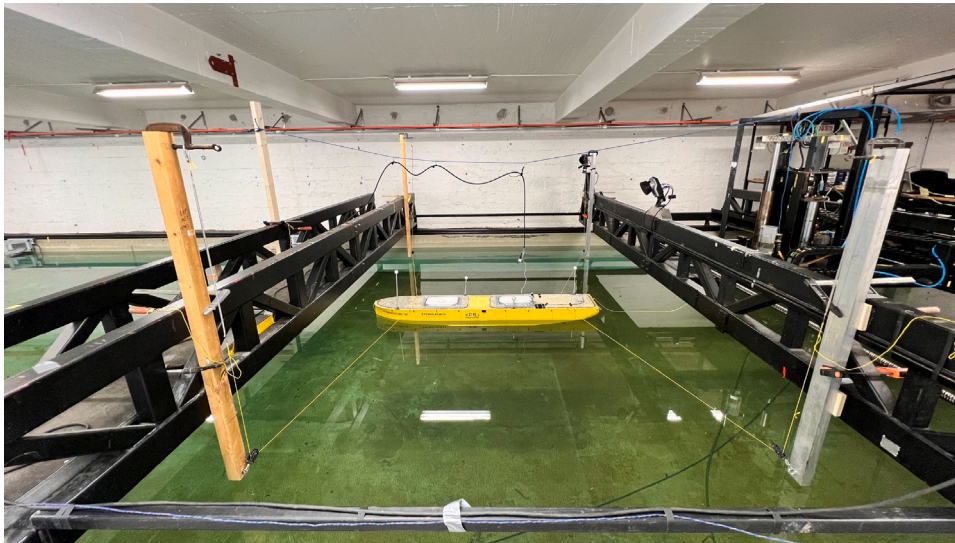
Fig. 5. The position and orientation of the model ship C/S Arctic Drillship (CSAD) were held fixed by a rope-pulley system.

4. Experimental validation of theory

4.1. Experimental design

The wave tank experiments were conducted in the NTNU marine cybernetics laboratory, which is a small wave basin with dimensions of 40 m × 6.45 m × 1.5 m. The laboratory is equipped with a wave maker, towing carriage, and real-time positioning system, making it an excellent playground for model-ship testing in regular and irregular waves.[4] We used the same model ship as in Dirdal et al. (2022), i.e., a 1:90 scaled model C/S Arctic Drillship (CSAD) equipped with several IMUs. In the following subsections, we explain the design measures taken to ensure that the assumptions of Section 2.5 were not significantly violated during data collection.

4.1.1. Constant heading and forward speed

The model ship heading and position were confined by a rope-pulley system connecting the ship to a towing carriage (Fig. 5). Each rope was attached to a spring, allowing almost free motions in heave, roll, and pitch while limiting the surge, sway, and yaw motions. The ropes were interchanged and adjusted to produce the desired boat headings.

Constant forward speed was achieved by using the towing carriage to pull the ship through the water. We considered three different carriage speeds, 0.5 m/s, 0.6 m/s, and 0.7 m/s, which, in full-scale, correspond to 9.1 knots, 11.1 knots, and 12.8 knots (using Froude scaling with 1:90 model scale), and are within the range of average transit speeds typical for drillships. Due to the limited length of the wave basin, these speeds could not be sustained by the towing carriage for more than 40 s in the slowest speed trial and less than 30 s in the highest speed trial. Consequently, the duration of all the recorded IMU data with forward speed is less than 40 s.

Due to the narrowness of the wave basin, only head sea ($\beta = 180°$) and following sea ($\beta = 0°$) conditions could be tested in the forward speed trials. Some oscillations in the heading angle of the ship were observed during experiments due to the towing carriage, impact of waves, and rope-pulley system. In order to assess the deviation caused by these oscillations, the real-time heading angle was measured using a separate camera-based positioning system called Qualisys. The measurements reported by Qualisys showed that the maximum error

between the initial heading and heading during experiments was less than 5°. To ensure that the results were minimally affected by such deviations, the true wave encounter angle was based on the average heading angle computed from the Qualisys heading measurements.

4.1.2. Wave period and wave height

The experimental wave periods were generally selected above the CSAD lower wave period threshold $T_{\min} = 1/f_{\max} \approx 1.3$ s (computed by inserting the CSAD length and breadth dimensions, $L = 2.58$ m and $B = 0.44$ m, with a water pool depth of 1.45 m into Eq. (20)) to reduce the effect of vessel filtering on the IMU data. However, regular wave experiments were conducted with a wave period of $T_p = 1.0$ s to demonstrate the issues related to high-frequency waves.

In general, as long as the vessel can "feel" the waves passing through it, Theorem 1 is valid irrespective of how small or tall the waves are. In practice, however, higher waves imply a higher signal-to-noise ratio (SNR) in the IMU measurements, which can improve estimation results. Despite the advantage of a high SNR, considerable wave heights posed challenges to our rope-pulley system causing large oscillations in the heading angle of the CSAD. Moreover, significant waves caused more water exposure on deck, increasing the risk of water leaking into the vessel and damaging electronics. For these reasons, only slight, moderate, and (to some extent) rough sea states were considered in the experiments (Table 2).

4.1.3. Sensor configuration

We equipped the CSAD with four Bosch BMI160 IMUs to record the vessel motions caused by waves. The IMUs were fastened to the vessel using Velcro tape and the array configuration is illustrated in Fig. 6(a): The sensor array is noncollinear, with $\{s_1\}$, $\{s_2\}$, and $\{s_3\}$ being almost coplanar and $\{s_4\}$ significantly elevated compared to the rest. The IMUs are all connected to a Raspberry Pi 3 Model B+ through a common serial bus using the I2C communication protocol. The individual IMU measurements were time-synchronized based on the internal clock of the Raspberry Pi. The IMU sampling rate was set to 50 Hz for all experiments as the serial bus could not handle the increased information load associated with higher sampling rates.

Unfortunately, Bosch does not provide any information about the in-run bias stability of the accelerometers and gyroscopes in the BMI160 IMU, meaning it is difficult for us to assess whether the biases remain constant or not within the time frame of the recorded data segments. However, it is plausible that the IMU data collected during forward speed were not significantly affected by the bias due to the short time

Table 2

The peak wave periods (T_p) considered in the experiments, along with the corresponding wave height H (regular waves) and significant wave height H_s (irregular waves). Numbers outside parentheses represent the actual model-scale experimental parameters, whereas numbers inside parentheses represent the equivalent full-scale parameters (obtained using Froude scaling with scale factor 90). All scaled wave heights can be characterized as either a slight, moderate, or rough sea state (Price and Bishop, 1974) with wave periods within the frequency range of wind-generated waves. Wave periods and wave heights are given in seconds and meters, respectively.

T_p	1.0 (9.5)	1.4 (13.3)	1.5 (14.2)	1.6 (15.2)	1.8 (17.1)	2.0 (19.0)	2.5 (23.7)
H	0.040 (3.56)	–	0.027 (2.43)	–	–	0.017 (1.53)	0.011 (1.03)
H_s	–	0.027 (2.43)	–	0.018 (1.63)	0.017 (1.53)	0.014 (1.29)	–

Table 3

Absolute phase difference errors $\bar{\Theta}_{ij}$ between our phase difference model (12) and the FFT estimated phase difference between the processed z-accelerations of IMUs $\{s_i\}$ and $\{s_j\}$ configured according to Fig. 6(a). The errors were evaluated for various sensor pairs exposed to regular waves with wave periods T_p = 1.0 s, 1.5 s, 2.0 s, and 2.5 s and vessel speeds U = 0.5 m/s, 0.6 m/s, and 0.7 m/s. The top and bottom tables show results for following sea ($\beta = 0°$) and head sea ($\beta = 180°$), respectively. All values are given in degrees.

T_p	U = 0.5 m/s				U = 0.6 m/s				U = 0.7 m/s			
	$\bar{\Theta}_{12}$	$\bar{\Theta}_{13}$	$\bar{\Theta}_{24}$	$\bar{\Theta}_{34}$	$\bar{\Theta}_{12}$	$\bar{\Theta}_{13}$	$\bar{\Theta}_{24}$	$\bar{\Theta}_{34}$	$\bar{\Theta}_{12}$	$\bar{\Theta}_{13}$	$\bar{\Theta}_{24}$	$\bar{\Theta}_{34}$
1.0 s	147.75	150.61	283.82	286.68	119.76	118.77	235.21	234.23	151.67	153.07	298.31	299.71
1.5 s	5.72	6.78	36.70	35.64	4.61	5.36	37.76	37.01	4.29	2.95	39.32	40.65
2.0 s	0.55	0.10	13.58	12.94	1.77	2.69	11.97	11.05	0.22	0.65	14.75	13.88
2.5 s	0.66	1.22	4.87	4.31	0.47	0.41	6.06	5.17	0.72	0.16	4.50	5.06

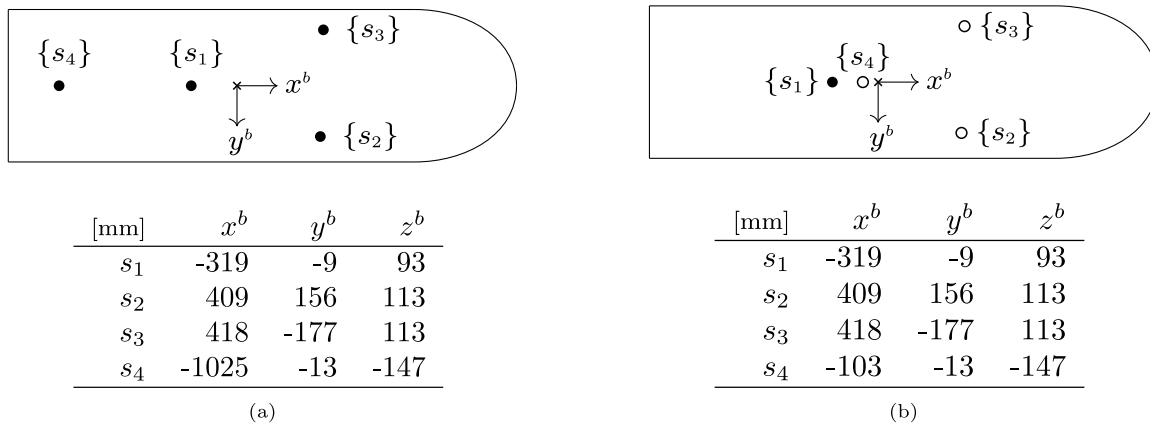| T_p	U = 0.5 m/s				U = 0.6 m/s				U = 0.7 m/s			
	$\bar{\Theta}_{12}$	$\bar{\Theta}_{13}$	$\bar{\Theta}_{24}$	$\bar{\Theta}_{34}$	$\bar{\Theta}_{12}$	$\bar{\Theta}_{13}$	$\bar{\Theta}_{24}$	$\bar{\Theta}_{34}$	$\bar{\Theta}_{12}$	$\bar{\Theta}_{13}$	$\bar{\Theta}_{24}$	$\bar{\Theta}_{34}$
1.0 s	103.35	108.24	230.45	235.33	106.01	108.75	230.45	233.19	108.01	106.72	234.41	233.12
1.5 s	0.33	0.22	37.77	37.22	2.49	2.43	34.34	34.40	4.35	4.29	30.53	30.60
2.0 s	1.95	1.55	15.23	14.83	3.13	2.59	16.78	16.23	5.27	4.48	21.21	20.43
2.5 s	2.21	2.20	9.91	9.90	1.38	0.93	9.10	8.65	2.19	2.57	9.29	9.68

Fig. 6. The IMU array configurations considered in the wave tank experiments. IMUs 1, 2, 3, and 4 are denoted $\{s_1\}$, $\{s_2\}$, $\{s_3\}$, and $\{s_4\}$, respectively. The location of each sensor is given in millimeters with respect to the vessel body frame $\{b\}$. The origin of $\{b\}$ is indicated by a cross and defined midships with the z-axis pointing down (into the page). The sensor configuration in (a) shows the original configuration of physically interconnected IMUs (filled circles), whereas (b) shows the virtual sensor configuration where only IMU 1 is physical and the locations of the other IMUs are virtual (hollow circles).

duration of all experiments (less than 40 s). On the other hand, the duration of the IMU data collected at zero speed was around 120 s, which may have been affected to a greater extent by the bias instability.

4.2. Results and discussion

In this section, we assess the validity of the theory developed in Section 2.5 by considering IMU data collected from experiments conducted in the wave basin where the model ship was stationary and underway in both regular and irregular waves. Since the time durations of the collected IMU data were short, we consider each complete time series as a single input data segment to our wave estimation algorithm (Algorithm 3). In the following results, the reference wave number was computed using the dispersion relation (21) along with the pool depth d = 1.45 m and the true peak wave period (i.e., the wave period used as input to the wavemaker machine). The peak wave period value was confirmed by examining the frequency content of the wave elevation data obtained from several wave probes placed around the tank. The reference wave propagation angle was obtained by fixing the ropes

of the model ship to produce the desired boat headings (Fig. 5) and confirming this value with the Qualisys camera system. In the following results, we refer to the wave propagation angle relative to the boat heading as the wave encounter angle when the vessel moves and the wave direction when the vessel is stationary.

4.2.1. Experimental validation of Assumption 1

We can assess the validity of Assumption 1 by comparing the phase differences predicted by Eq. (12) with the actual phase differences measured between the sensors on the vessel for a range of vessel speeds, wave periods, and wave directions. The error between the phase differences (Table 3) reveal three interesting observations: (i) the phase errors associated with wave period T_p = 1.0 s are disproportionately large compared to the other wave periods, (ii) the sets of phase errors $\{\bar{\Theta}_{12}, \bar{\Theta}_{13}\}$ are smaller than $\{\bar{\Theta}_{24}, \bar{\Theta}_{34}\}$ for all experiments, and (iii) the errors generally decrease with increasing wave period.

The extreme deviations in observation (i) are caused by vessel filtering, which (in this case) occurs whenever the wave period is roughly
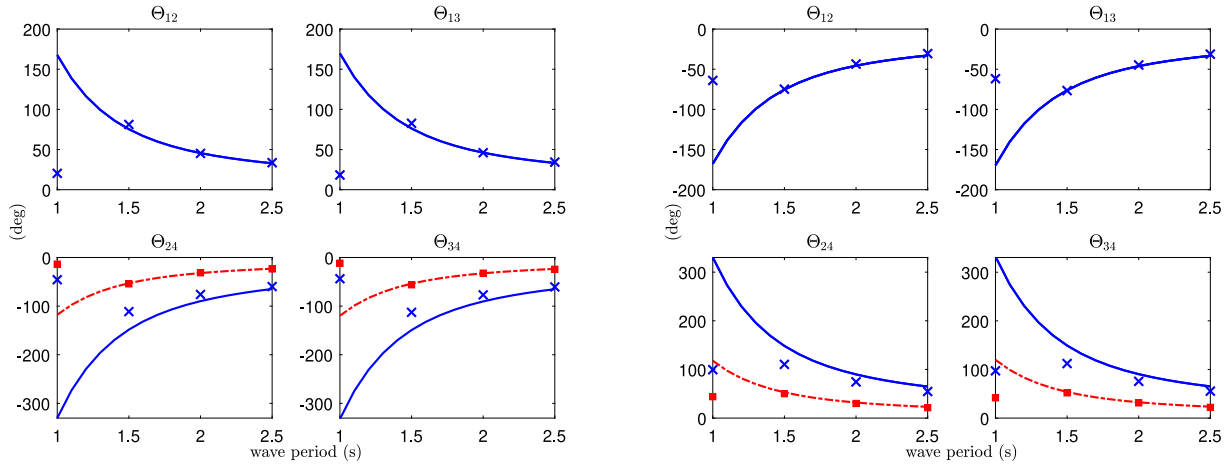
Fig. 7. The phase differences predicted by our model (12) (solid blue line) vs. the "true" phase differences (blue crosses) between respective sensor pairs as a function of wave period for vessel speed $U = 0.5$ m/s. The "true" phase differences were obtained by applying an FFT to the processed z-accelerations of each IMU to get the corresponding phase values. The results in red (dashed-dotted curves and squares) show the corresponding phase differences after virtually moving IMU 4 closer to the other IMUs. This virtual placement was achieved by employing the measurement transformation (19) and the modified sensor configuration in Fig. 6(b), together with the processed linear accelerations, angular rates, and angular accelerations of IMU 1. The dashed-dotted line shows the predicted phase differences (12) based on the new sensor location, whereas the squares show the corresponding "true" phase differences obtained using an FFT as before. Left and right-handed plots show results for following sea ($\beta = 0°$) and head sea ($\beta = 180°$), respectively. The phase difference results for $U = 0.6$ m/s and 0.7 m/s have been omitted as they were almost identical to the results displayed.

less than 1.3 s.[5] When the waves are sufficiently short, the vessel acts as a lowpass filter and attenuates the waves passing through it, resulting in a reduction in the angular rates of the body. A reduction in the angular rates causes the rigid-body accelerations to become increasingly similar (see Eq. (6)), which, in turn, implies that the phase differences approach zero. However, the phase differences predicted by Eq. (12) generally increase with decreasing wave period as it does not consider a rigid body. These opposite behaviors result in a growing deviation between the true phase difference dynamics and our proposed model (Fig. 7). As the wave period decreases, the true phase differences will approach zero due to vessel lowpass filtering becoming increasingly dominant, whereas the predicted phase differences continue to infinity.

The noticeable difference between the sets of phase errors in observation (ii) is mainly caused by a difference in the separation distance between sensors $\{s_1, s_2, s_3\}$ and $\{s_2, s_3, s_4\}$ (Fig. 6(a)). Specifically, the x-coordinate of $\{s_4\}$ is significantly larger than $\{s_2\}$ and $\{s_3\}$, which induces a larger deviation between the estimated and actual phase differences associated with $\{s_4\}$. However, if we bring $\{s_4\}$ closer to the other sensors, the deviation decreases to zero (Fig. 7). As explained in Section 2.1, we expect Eqs. (6) and (12) to yield roughly the same phase difference when the separation is sufficiently small since both models are proportional to the sensor separation. It is worth stressing, however, that there is generally a lower limit on how close the sensors may be separated before the state-space model loses observability. As the sensor separations decrease, there is an increasing risk that the measured phase differences all become zero, meaning there is no longer any guarantee that the UKF algorithm will find the correct solution. However, it is difficult to quantify the minimum sensor separation as it depends on the sensor sampling rate and speed/frequency of the waves passing through the sensors. Since the sampling rate is considered fixed for the system, a speed/frequency will always exist where the waves will appear without delay in all sensors, irrespective of the given sensor separation. Hence, the sensor separations should not be considered a fixed universal quantity but rather tunable parameters that can be adapted to different wave conditions. For instance, one possible strategy is to consider different sets of sensor separations, each of which should be applied depending on the measured wave frequency

given by the FFT. However, a methodology based on such a strategy is outside the scope of the present study and left as a potential application for future work.

Observation (iii) can be understood by studying the effect of increasing the wave period on the models (6) and (12). The phase difference in Eq. (12) is proportional to the wave number, which, in turn, is inversely proportional to the wave period. Thus, as the wave period increases, the predicted phase difference generally decreases towards zero (Fig. 7). The effect of increasing the wave period on the angular rates and accelerations in Eq. (6) can be understood by considering the vessel roll and pitch responses in regular waves, which, for an underway vessel, can generally be expressed as

$$\phi(t) = A_\phi \sin(\omega_e t + \epsilon_\phi),$$
$$\theta(t) = A_\theta \cos(\omega_e t + \epsilon_\theta), \tag{36}$$

where A_ϕ and A_θ denote the roll and pitch amplitudes, ω_e is the wave encounter frequency, and ϵ_ϕ and ϵ_θ represent the phase shifts. Assuming that the boat heading is fixed (i.e., $\dot{\psi} = 0$), the angular rates p and q can be written mathematically as $p = \dot{\phi}$ and $q = \dot{\theta} \cos(\phi)$ (Fossen, 2021). Computing the time derivatives of Eq. (36) we see that the amplitudes of p and q depend directly on ω_e. Hence, as the wave period increases, the angular frequencies ω and ω_e will be driven to zero, further implying that p, q, $\dot{p}$, and $\dot{q}$ will also converge to zero. The latter result makes intuitive sense as, for very long waves, the vessel will appear to oscillate up and down vertically, with little roll and pitch motion, causing the measurements in each sensors to be almost identical (i.e., zero phase difference). Therefore, it is clear that increasing the wave period will cause both models (6) and (12) to converge to zero, which, in turn, implies that the corresponding error between them will behave in a similar fashion.

Unfortunately, due to the size of the wave tank, it was not possible to assess the validity of Assumption 1 for other boat headings in forward speed. Nevertheless, we carried out similar experiments in regular waves for the stationary case (i.e., $U = 0$ m/s) with boat headings $\{0°, 30°, 60°, 90°, 120°, 150°, 180°\}$ and obtained similar results. Hence, based on these experimental results, it is reasonable to conclude that Assumption 1 is valid.

4.2.2. Experimental validation of Theorem 1

The experimental results associated with the set of phase differences $\{\Theta_{12}, \Theta_{13}\}$ (Tables 4 and 5) show that in 89% and 83% of experiments considered with the original IMU setup, the wave encounter

---

[5] This value was obtained by evaluating Eq. (15) with $\beta = 0°/180°$ and $L = 2.58$ m, equating it with $\lambda = 2\pi/k$, and finding corresponding the wave period.

Table 4

Wave encounter angle results associated with the pairs of phase differences $\{\Theta_{12}, \Theta_{13}\}$ and $\{\Theta_{24}, \Theta_{34}\}$, respectively, for wave periods $T_p = 1.5$ s, 2.0 s, and 2.5 s and vessel speeds $U = 0.5$ m/s, 0.6 m/s, and 0.7 m/s in regular waves. The numbers represent the absolute error between the wave angle estimates (after convergence) from our wave algorithm (Algorithm 3) and the true values. Numbers outside parentheses represent errors associated with the original sensor configuration (Fig. 6(a)), where all results are based on physical IMU data. Numbers inside parentheses represent errors associated with a single physical IMU. The latter errors were obtained by using the processed linear acceleration, angular rates, and angular acceleration of IMU 1 with the measurement transformation (19) and the virtual sensor configuration in Fig. 6(b) to generate the other IMU measurements. The top and bottom tables show the results for following sea ($\beta = 0°$) and head sea ($\beta = 180°$), respectively. All wave angle errors are given in degrees.

T_p	$U = 0.5$ m/s		$U = 0.6$ m/s		$U = 0.7$ m/s	
	$\{\Theta_{12}, \Theta_{13}\}$	$\{\Theta_{24}, \Theta_{34}\}$	$\{\Theta_{12}, \Theta_{13}\}$	$\{\Theta_{24}, \Theta_{34}\}$	$\{\Theta_{12}, \Theta_{13}\}$	$\{\Theta_{24}, \Theta_{34}\}$
1.5 s	4.92 (2.47)	7.26 (2.43)	1.34 (0.58)	1.15 (0.53)	3.94 (2.32)	3.29 (2.40)
2.0 s	2.06 (1.77)	2.70 (1.77)	4.37 (2.35)	5.91 (2.31)	6.43 (2.35)	7.14 (2.27)
2.5 s	0.14 (2.06)	0.41 (2.05)	4.36 (3.36)	6.26 (3.35)	2.63 (3.75)	3.86 (3.75)
T_p	$U = 0.5$ m/s		$U = 0.6$ m/s		$U = 0.7$ m/s	
	$\{\Theta_{12}, \Theta_{13}\}$	$\{\Theta_{24}, \Theta_{34}\}$	$\{\Theta_{12}, \Theta_{13}\}$	$\{\Theta_{24}, \Theta_{34}\}$	$\{\Theta_{12}, \Theta_{13}\}$	$\{\Theta_{24}, \Theta_{34}\}$
1.5 s	1.74 (0.91)	3.02 (1.03)	0.17 (0.16)	1.10 (0.03)	4.14 (0.09)	4.58 (0.14)
2.0 s	0.49 (1.23)	0.63 (1.27)	3.60 (1.76)	4.38 (1.80)	2.60 (2.72)	2.28 (2.71)
2.5 s	1.91 (0.22)	1.97 (0.21)	6.70 (1.86)	6.87 (1.83)	2.24 (1.30)	2.06 (1.29)

Table 5

Wave number results associated with the pairs of phase differences $\{\Theta_{12}, \Theta_{13}\}$ and $\{\Theta_{24}, \Theta_{34}\}$, respectively, for wave periods $T_p = 1.5$ s, 2.0 s, and 2.5 s and vessel speeds $U = 0.5$ m/s, 0.6 m/s, and 0.7 m/s in regular waves. The numbers represent the absolute error between the wave number estimates (after convergence) from our wave algorithm (Algorithm 3) and the true values. Numbers outside parentheses represent the wave number errors associated with the original sensor configuration (Fig. 6(a)), where all results are based on physical IMU data. Numbers inside parentheses represent the wave number errors associated with a single physical IMU. The latter errors were obtained by using the processed linear acceleration, angular rates, and angular acceleration of IMU 1 with the measurement transformation (19) and the virtual sensor configuration in Fig. 6(b) to generate the other IMU measurements. The top and bottom tables show the results for following sea ($\beta = 0°$) and head sea ($\beta = 180°$), respectively. All wave number errors are given in m^{-1}.

T_p	$U = 0.5$ m/s		$U = 0.6$ m/s		$U = 0.7$ m/s	
	$\{\Theta_{12}, \Theta_{13}\}$	$\{\Theta_{24}, \Theta_{34}\}$	$\{\Theta_{12}, \Theta_{13}\}$	$\{\Theta_{24}, \Theta_{34}\}$	$\{\Theta_{12}, \Theta_{13}\}$	$\{\Theta_{24}, \Theta_{34}\}$
1.5 s	0.17 (0.06)	0.40 (0.08)	0.09 (0.06)	0.46 (0.10)	0.10 (0.09)	0.48 (0.17)
2.0 s	0.02 (0.01)	0.14 (0.01)	0.10 (0.05)	0.13 (0.07)	0.07 (0.01)	0.14 (0.02)
2.5 s	0.02 (0.02)	0.03 (0.03)	0.05 (0.00)	0.07 (0.00)	0.04 (0.02)	0.08 (0.02)
T_p	$U = 0.5$ m/s		$U = 0.6$ m/s		$U = 0.7$ m/s	
	$\{\Theta_{12}, \Theta_{13}\}$	$\{\Theta_{24}, \Theta_{34}\}$	$\{\Theta_{12}, \Theta_{13}\}$	$\{\Theta_{24}, \Theta_{34}\}$	$\{\Theta_{12}, \Theta_{13}\}$	$\{\Theta_{24}, \Theta_{34}\}$
1.5 s	0.09 (0.00)	0.39 (0.08)	0.15 (0.06)	0.36 (0.04)	0.05 (0.07)	0.36 (0.08)
2.0 s	0.07 (0.04)	0.18 (0.05)	0.08 (0.07)	0.19 (0.08)	0.11 (0.11)	0.24 (0.11)
2.5 s	0.08 (0.05)	0.13 (0.05)	0.02 (0.03)	0.10 (0.02)	0.03 (0.06)	0.14 (0.06)

angle and wave number errors are less than 5° and 0.1 m^{-1}, respectively.[6] These numbers provide strong evidence in favor of Theorem 1 and extend previous findings by showing that the PTPD approach is valid for underway vessels and not only stationary ones (Udjus, 2017; Heyn et al., 2017; Dirdal et al., 2022). Unfortunately, due to the narrowness of the wave tank, it was not possible to assess Theorem 1 for other boat headings in forward speed. We refer to our previous work (Dirdal et al., 2022) for an assessment of Theorem 1 for boat headings $\{0°, 30°, 60°, 90°, 120°, 150°, 180°\}$ in the stationary case (i.e., $U = 0$ m/s). It is worth mentioning that we have omitted the results for wave period $T_p = 1.0$ s since Assumption 1 is violated for that period, as discussed in Section 4.2.1.

In contrast, the experimental results (Tables 4 and 5) also show that for the set of phase differences $\{\Theta_{24}, \Theta_{34}\}$, merely 83% and 22% of the total wave encounter angle and wave number errors are within 5° and 0.1 m^{-1}, respectively. The significant difference in quality (especially in the wave number) compared to the errors achieved using the set $\{\Theta_{12}, \Theta_{13}\}$ can be explained by a difference in the sensor positioning of $\{s_1, s_2, s_3\}$ and $\{s_2, s_3, s_4\}$. As discussed in Section 4.2.1, $\{s_4\}$ is displaced further from $\{s_2, s_3\}$ along the x^b axis than $\{s_1\}$, resulting

in a greater deviation between our phase difference model and the actual phase difference dynamics. Bringing $\{s_4\}$ closer to the other sensors reduces the deviation between the models, resulting in 100% and 94% of the wave encounter angle and wave number errors for $\{\Theta_{24}, \Theta_{34}\}$ being within 5° and 0.1 m^{-1} (Tables 4 and 5), respectively. It is worth stressing that although the deviation can in theory be reduced to zero by bringing the sensors very close, doing so in practice may compromise the observability of Eq. (13), as discussed in Section 4.2.1.

The wave number estimation results (Table 5) also demonstrate another interesting and beneficial fact: We can retain the absolute frequency (through the dispersion relation (21)) from shipboard IMU measurements taken in the encounter frequency domain. This property is particularly useful for beam to following sea conditions (i.e., $\beta \in (-90°, 90°)$) in which the wave encounter frequency generally does not possess a unique solution (Fig. 8). Due to the observability of our state-space model, our approach directly maps the phase differences (which are based on the encounter frequency) to the absolute frequency domain, thereby circumventing the 1-to-3 mapping problem associated with underway vessels in following seas (Nielsen, 2017b, 2018).

4.2.3. Experimental validation of Corollary 1.1

The experimental results (Tables 4 and 5) show that for a *single* IMU in 100% and 94% of experiments considered, the wave encounter angle and wave number errors are within 5° and 0.1 m^{-1}, respectively. These numbers extend previous findings by showing that a single IMU is sufficient, as opposed to three, as initially proposed in Dirdal et al. (2022). This result increases the practical utility of the PTPD approach

---

[6] For comparison, standard commercial radars such as Miros SM-050 and Miros Wavex report wave direction accuracies of 7° and 20° and wave period accuracies of 5% and 10%—see Table 6 for how these values affect the accuracy of the wave number and why 0.1 m^{-1} was selected as the accepted error threshold.

Table 6
Theoretical wave number errors $\tilde{k}$ (unit m^{-1}) resulting from a 5% and 10% error in the experimental wave periods T_p (unit seconds). The wave number errors were computed from Eq. (21) by adding and subtracting the percentage error to each respective wave period. In each calculation, the water pool depth of the wave basin ($d = 1.45$ m) was considered. Based on these numbers, we consider 0.1 m^{-1} a reasonable error threshold to assess the quality of the wave number estimation results.

T_p	1.0	1.4	1.5	1.6	1.8	2.0	2.5
$\tilde{k}_{5\%}$	0.40	0.20	0.17	0.15	0.11	0.09	0.05
$\tilde{k}_{10\%}$	0.82	0.41	0.35	0.30	0.23	0.18	0.11

significantly as many vessels already employ IMUs as part of their sensor suite, thus allowing the approach to be applied directly without the need for installing additional units and time synchronizing the measurements between them. It is worth emphasizing that the results presented here are only valid for IMUs, which can measure angular rates and specific force simultaneously—both of which Eq. (19) relies on.

However, an important drawback of Eq. (19) is that it depends on the angular acceleration $\dot{\boldsymbol{\omega}}_{nb}^b$, which is not usually measured. In this work, we have obtained estimates of the latter through numerical differentiation of $\boldsymbol{\omega}_{nb}^b$, which we argue is valid since each measurement data segment has been lowpass filtered (see Section 3.1.2). The validity of using numerical differentiation is further substantiated by our results, which are either similar in magnitude or outperform the results based on multiple physical IMUs. It is worth mentioning that there exist other methods for estimating $\dot{\boldsymbol{\omega}}_{nb}^b$ (Zappa et al., 2001; Kjerstad and Skjetne, 2016); however, these rely on an array of (minimum) four noncoplanar tri-axial accelerometers.

It is interesting to see that the wave estimates for $\{\Theta_{12}, \Theta_{13}\}$ from a single IMU, in many cases, produce lower errors than for three physical IMUs (Tables 4 and 5), despite the sensor coordinates being (in theory) the same. We speculate that one of the reasons for this behavior is that the application of Eq. (19) effectively eliminates any bias resulting from uncertainties in the sensor positioning. As discussed in Dirdal et al. (2022), uncertainties in the sensor positions can result in significant errors in the phase differences, especially for higher frequency waves. By employing Eq. (19) instead, the issues regarding sensor positioning are conveniently circumvented, as any virtual sensor coordinates specified as input to Eq. (19) represents the true location.

Up to now, we have used Eq. (19) to generate the *minimum* number of measurements needed to determine the wave encounter angle and wave number uniquely. However, it is worth pointing out that we could use Eq. (19) to spawn any arbitrary number of measurements. As discussed in Dirdal et al. (2022), increasing the number of phase differences will reduce the error variance of the estimates, but only up to a specific limit. Note that this will only work if the virtual sensor locations are noncollinear (Theorem 1) and sufficiently close to each other (Assumption 1).

4.2.4. Long-crested irregular waves

So far, we have established the theoretical foundation for determining the wave encounter angle and wave number from a train of regular harmonic waves. However, in reality, ocean waves are irregular, typically characterized by many wave components differing in amplitude, frequency, and wave direction. For *long-crested* irregular waves, each constituent wave component has the same propagation direction, meaning that it is, in theory, sufficient only to consider one such wave component to infer the general propagation direction. Hence, if we can extract only one wave component/frequency (e.g., using an FFT), we can apply Theorem 1 and Corollary 1.1 to determine the wave propagation direction of long-crested irregular waves from a single IMU.

In order to assess the validity of the approach mentioned above, two sets of experiments were conducted in the wave basin involving a stationary and underway vessel, respectively, subjected to long-crested irregular waves. In the stationary and forward speed trials, we considered the set of boat headings $\{0°, 30°, 60°, 90°, 120°, 150°, 180°\}$
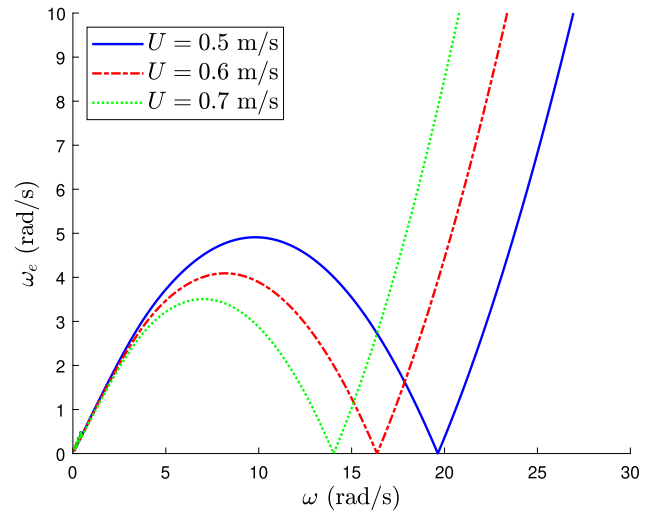

Fig. 8. Encounter wave frequency (ω_e) vs. absolute wave frequency (ω) in following waves ($\beta = 0°$) computed by Eq. (22) with water depth $d = 1.45$ m (results are almost identical for increasing d) and forward vessel speeds $U = 0.5$ m/s, 0.6 m/s, and 0.7 m/s to represent the test conditions of the wave basin. When $\omega_e < 1/4\psi$, where $\psi = U\cos\beta/g$, the wave encounter frequency maps to three different (absolute) wave frequencies. The latter situation applies for all our experiments conducted in following waves with (absolute) wave periods $T_p = 1.5$ s, 2.0 s, and 2.5 s.

and $\{0°, 180°\}$, respectively, with significant wave heights and peak wave periods given in Table 2. The experimental results (Tables 7 and 8) show that in 92% of the forward speed trials and 79% of the stationary trials, the wave encounter angle error is less than 5°. If we extend the error threshold to 10°, all wave direction estimates except one are within the latter. These results demonstrate that our phase difference model can also be applied to long-crested irregular waves to uniquely resolve the relative wave propagation direction from a single IMU. The application of our approach to long-crested irregular waves for stationary and underway vessels extends previous works (Udjus, 2017; Heyn et al., 2017; Dirdal et al., 2022), which are limited to a stationkeeping vessel and regular waves, and whose results are based on multiple physical IMUs.

Despite the good agreement between the wave direction results, the same level of agreement is not seen for the wave number, which, for underway and stationkeeping trials, yields 71% and 57% of errors less than 0.1 m^{-1} (Tables 7 and 8), respectively. It is difficult to state with certainty the exact reasons for the observed discrepancies; however, we speculate that they are caused by a combination of (i) poor frequency resolution in the FFT spectra, (ii) a growing mismatch between our phase prediction model and the true vessel dynamics due to increased angular vessel rates, and (iii) the UKF algorithm sometimes favoring a low wave direction error at the expense of a high wave number error. Each of these issues are addressed in the following paragraphs.

As mentioned in Section 4.1, the time duration of the recorded IMU data was less than 40 s for the forward speed trials and less than 120 s for the zero speed trials. Time durations of such magnitudes will invariably impact the attainable frequency resolution of the FFT spectra. As discussed in Section 3.4.3, a poor frequency resolution will make it more challenging to pinpoint the true frequency, causing it

Table 7

Wave encounter angle and wave number results, $\tilde{\beta}$ and $\tilde{k}$, respectively, from forward speed trials in following and head waves (i.e., $\beta = 0°$ and $\beta = 180°$) with vessel speeds $U = 0.5$ m/s, 0.6 m/s, and 0.7 m/s exposed to long-crested irregular waves with peak wave periods $T_p = 1.4$ s, 1.6 s, 1.8 s, and 2.0 s. The numbers show the absolute error between the wave estimates (after convergence) from our wave algorithm (Algorithm 3) and the true values by considering the set of phase differences $\{\Theta_{12}, \Theta_{13}, \Theta_{14}, \Theta_{23}, \Theta_{24}, \Theta_{34}\}$ and the virtual sensor configuration in Fig. 6(b). Note that in the results presented we have reduced the maximum frequency threshold in Algorithm 3 to $f_{max} = 0.6$ Hz. The wave encounter and wave number errors are given in degrees and m^{-1}, respectively.

T_p	$U = 0.5$ m/s				$U = 0.6$ m/s				$U = 0.7$ m/s			
	$\beta = 0°$		$\beta = 180°$		$\beta = 0°$		$\beta = 180°$		$\beta = 0°$		$\beta = 180°$	
	$\tilde{\beta}$	$\tilde{k}$	$\tilde{\beta}$	$\tilde{k}$	$\tilde{\beta}$	$\tilde{k}$	$\tilde{\beta}$	$\tilde{k}$	$\tilde{\beta}$	$\tilde{k}$	$\tilde{\beta}$	$\tilde{k}$
1.4 s	0.19	0.47	1.95	0.03	0.37	0.49	7.44	0.05	2.28	0.08	6.35	0.06
1.6 s	0.39	0.15	0.14	0.06	0.40	0.24	0.47	0.15	4.18	0.71	2.30	0.01
1.8 s	1.88	0.06	0.05	0.06	1.68	0.12	1.86	0.05	2.93	0.00	0.19	0.09
2.0 s	0.11	0.06	0.11	0.02	0.91	0.02	4.61	0.02	3.13	0.07	2.40	0.06

Table 8

Wave direction and wave number results, $\tilde{\beta}$ and $\tilde{k}$, respectively, from a stationary vessel exposed to long-crested irregular waves with peak wave period $T_p = 1.4$ s, 1.6 s, 1.8 s, and 2.0 s and wave directions $\beta = 0°$, 30°, 60°, 90°, 120°, 150°, and 180°. The numbers show the absolute error between the wave estimates (after convergence) from our wave algorithm (Algorithm 3) and the true values by considering the set of phase differences $\{\Theta_{12}, \Theta_{13}, \Theta_{14}, \Theta_{23}, \Theta_{24}, \Theta_{34}\}$ and the virtual sensor configuration in Fig. 6(b). Note that in the results presented we have reduced the maximum frequency threshold in Algorithm 3 to $f_{max} = 0.6$ Hz. The wave direction and wave number errors are given in degrees and m^{-1}, respectively.

T_p	$\beta = 0°$		$\beta = 30°$		$\beta = 60°$		$\beta = 90°$		$\beta = 120°$		$\beta = 150°$		$\beta = 180°$	
	$\tilde{\beta}$	$\tilde{k}$	$\tilde{\beta}$	$\tilde{k}$	$\tilde{\beta}$	$\tilde{k}$	$\tilde{\beta}$	$\tilde{k}$	$\tilde{\beta}$	$\tilde{k}$	$\tilde{\beta}$	$\tilde{k}$	$\tilde{\beta}$	$\tilde{k}$
1.4 s	1.89	0.20	3.45	0.03	2.06	0.26	2.46	0.01	3.85	0.05	6.51	0.08	0.87	0.17
1.6 s	0.92	0.24	7.56	0.01	1.72	0.42	3.83	0.08	3.14	0.19	10.47	0.06	0.18	0.10
1.8 s	1.57	0.11	6.91	0.28	4.00	0.11	2.90	0.13	3.55	0.22	5.56	0.06	0.90	0.07
2.0 s	0.41	0.10	3.10	0.04	3.13	0.09	2.92	0.06	2.80	0.01	9.58	0.14	0.92	0.02

to fall between two frequency bins and ultimately affecting the phase response. In order to improve FFT resolution, a longer FFT length must be considered, which may be fulfilled by increasing the duration of the measured data or by various interpolation techniques such as zero-padding.

Inspecting the wave estimation errors in Table 8 closely, it is clear that the most significant wave direction and wave number errors are associated with the experiments in which $\beta = 30°, 60°, 120°$ and 150°. In those experiments, we expect the angular rates of the body to be quite high due to the vessel roll and pitch responses being active and large simultaneously (the waves are approaching the vessel diagonally as opposed to straight on or from the side). An increase in the angular rates will cause a growing mismatch between our phase prediction model and the actual phase difference dynamics. As discussed in Section 4.2.1, this mismatch can generally be reduced by tuning the sensor separations such that the virtual sensor positions become sufficiently close.

The issues raised above will manifest themselves as errors in the estimated phase differences. These errors tend to be reflected more in one of the wave quantities than the other and less often in both simultaneously. In other words, when significant errors are present, the UKF algorithm seems to favor a lower estimation error in one of the wave quantities at the expense of a higher error in the other. In order to assess this speculation, we have conducted a small simulation study investigating how individual estimation errors are affected by the UKF for a range of wave directions and frequencies when significant errors in the phase differences are present. In addition to confirming the speculation above, the results (Fig. 9) also show that the wave number error is generally more sensitive to changes in the wave period (compare the magnitudes of the wave direction and wave number errors in the plots in Fig. 9). This behavior can explain some of the opposing wave estimation results in Tables 7 and 8 and, in particular, why the wave number error in some cases appears to be affected more than the corresponding wave direction error.

It is worth mentioning that in the results presented (Tables 7 and 8), we have reduced the maximum frequency threshold f_{max} in Algorithm 3, which produced better results. As we have seen, lower frequencies (longer wave periods) tend to produce more accurate wave estimates due to a reduction in the angular rates of the body, thus yielding less mismatch between our model and the actual vessel dynamics. However, by reducing the frequency threshold, our algorithm may effectively select a frequency different from the spectrum's peak frequency. This operation poses no issue for long-crested seas as each wave component propagates in the same direction. However, for more short-crested seas where multiple propagation directions may exist, care must be exercised to maintain the frequency threshold so that the desired peak wave frequency and direction are addressed.

5. Full scale experiments

5.1. Experimental design

During spring 2022, an experimental campaign was carried out with the NTNU-owned research vessel Gunnerus (Fig. 10) in the vicinity of Ålesund, a small coastal city on the west coast of Norway, to collect full-scale IMU data in various sea states and to assess the practicality of our proposed PTPD method. The research vessel Gunnerus is equipped with an advanced dynamical positioning system and many other instruments, making it an excellent platform for measuring waves at zero and forward speed.[7]

5.1.1. Campaign description

The field experiments were conducted over the course of two days. On each of these days, experiments involving zero and forward speed were, respectively, considered. The zero-speed trials were carried out in two distinct locations (Fig. 11(a)) in which the vessel was exposed to open and sheltered waters, respectively. At each location, four heading angles were considered by orienting the vessel into the waves (head sea) and subsequently adjusting the heading angle by 30°. Each heading angle and vessel position was maintained for approximately 40 min by the dynamical positioning system onboard. However, the duration of some experiments is shorter since the data logging system had to be restarted for some experiments, resulting in a loss of data. The forward

---

[7] For more information and details about the vessel and the equipment onboard, the reader is referred to the official Gunnerus website: https://www.ntnu.edu/oceans/gunnerus.
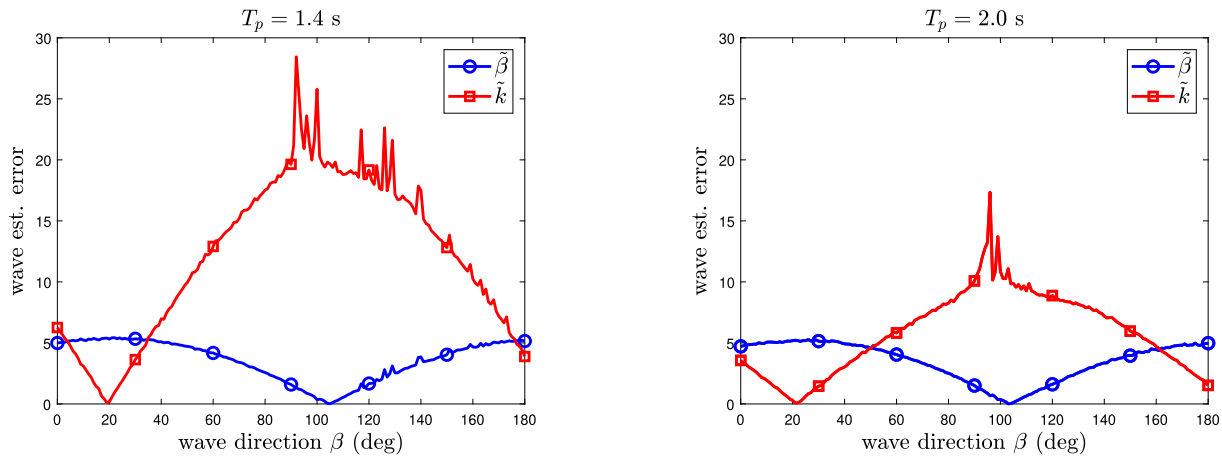
Fig. 9. Wave direction and wave number estimation results from our UKF algorithm (Algorithm 2) based on simulated phase differences with added random Gaussian noise. The phase differences were simulated using Eq. (12) with the sensor configuration in Fig. 6(b) and adding random Gaussian noise with mean 10° and standard deviation 5° to the computed values. The set of phase differences $\{\Theta_{12}, \Theta_{13}, \Theta_{14}, \Theta_{23}, \Theta_{24}, \Theta_{34}\}$ were considered in the simulation together with wave periods $T_p = 1.4$ s (left) and $T_p = 2.0$ s (right). The plots show the absolute error between the wave estimates (after convergence) and the true values. The wave direction error is given in degrees, whereas the wave number error is given in m^{-1} but multiplied by a factor of 100 to better highlight the overall trend.

Fig. 10. The research vessel Gunnerus considered in the full-scale experiments.

speed trials consist of a single experiment in head sea (Fig. 11(b)) lasting approximately 6 min. The short time duration and the limited number of trials for forward speed were due to ship operational issues.

5.1.2. IMU system and sensor configuration

Our data logging system comprises five ADIS16465 high-precision microelectric mechanical system (MEMS) IMUs (each of which includes a tri-axial accelerometer and gyroscope), a GPS receiver, a solid state drive, and a synchronization unit (Fig. 12). The IMUs and GPS receiver are all connected to the synchronization unit, which performs the synchronization of measurements using PPS time synchronization. All communication between the IMU nodes is done serially through the SPI protocol via cables of length 20 m. For all experiments, the IMU sampling rate was set to 100 Hz. We consider this sampling rate sufficient, as it is twice the rate used for the wave tank experiments as well as much higher than the bandwidth of wind-generated ocean waves.

The IMUs were rigidly attached to the vessel by clamping them onto the metal bars running across the roof of Gunnerus using screw clamps (Fig. 13). The metal bars run laterally across the vessel, making them an excellent reference to ensure that the gyroscope/accelerometer x-axis of each IMU is aligned with the vessel's longitudinal axis (thus minimizing

potential misalignment errors). The distances between the IMUs were measured using a laser distance measure tool relative to a common and known reference point on the vessel.

The IMU configuration considered in experiments is illustrated in Fig. 14. The IMU array is noncollinear and coplanar. The former is necessary to ensure that the state-space model (13) is observable, whereas the latter reduces the deviation between Eqs. (11) and (12) when $z_{ij} = 0$ (see Appendix). The sensor positions were deliberately chosen to be near each other for three reasons. First, as established in Section 4.2.1, Assumption 1 is valid when the sensors are sufficiently close to each other. Second, the rigid-body assumption is preserved more for smaller regions on the vessel than positions on opposite ends (e.g., bow and stern), which are more susceptible to bending and other forms of deformation. Third, no other locations were as suitable as the roof for measuring distances and fastening the sensors to the vessel (drilling into the vessel to attach the sensors was not permitted).

The gyroscope and accelerometer sensor biases were assumed constant for the duration of each processed data segment. This assumption is substantiated by the gyroscope and accelerometer Allan variance curves found in the ADIS16465 datasheet, which states that for a 6 min integration period (the considered window length of each data segment; see Section 5.2.1 for discussion), the gyroscope and accelerometer in-run bias stability are less than 2°/hr and 4.5 μg, respectively.

5.1.3. Wave direction reference systems

Gunnerus possesses a commercial wave radar system comprising a Furuno X-band marine radar and a Miros Wavex computer. The Miros computer processes the raw Furuno radar images of backscattered light reflected off the sea surface to produce estimates of the directional wave spectrum. In the following results, we consider the main/dominant wave direction estimated by the wave radar system as the ground truth reference value. Moreover, we consider the accepted wave direction error threshold to be 20° when evaluating the performance of our wave estimation algorithm, as this number is the wave direction accuracy reported by the Miros Wavex system.

Some of the zero-speed experiments were performed near a Fugro Seawatch Wavescan buoy (Fig. 11(a)) owned and administered by the Norwegian Public Roads Administration, who has made the buoy data available to the public (Furevik et al., 2016). The buoy measures almost everything related to the sea surface, including directional information, rendering it an additional useful reference for wave assessment. Compared to the wave radar system, however, the update rate of the buoy is significantly lower, with updates given every 10 min as opposed to 1 min for the wave radar.
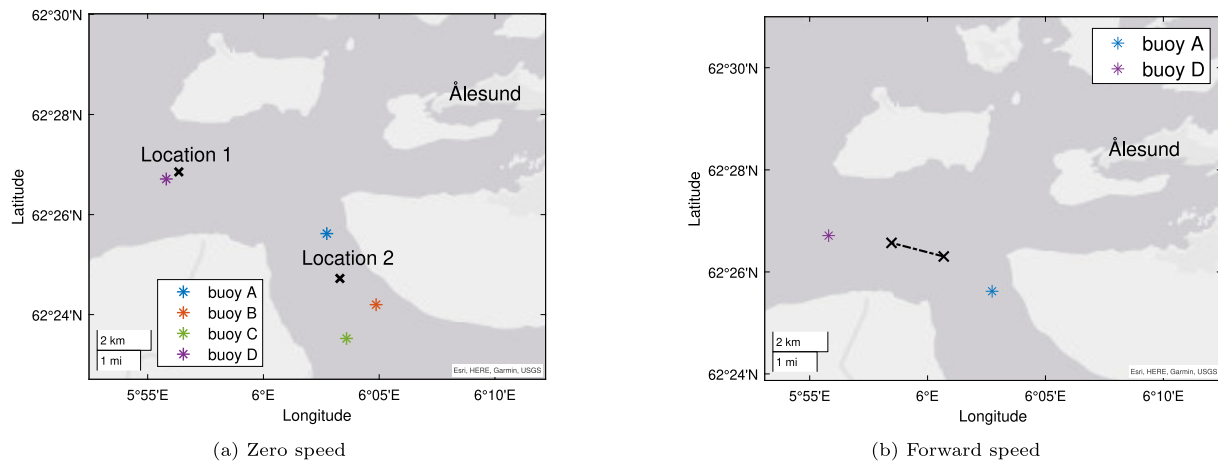
(a) Zero speed

(b) Forward speed

Fig. 11. The zero-speed trials were conducted in two distinct locations: Breidsundet (Location 1) and Sulafjorden (Location 2). The forward speed trials comprise only one experiment because of ship operational issues, bringing the campaign to an abrupt end. Several directional wave rider buoys are stationed in the region, which the Norwegian Public Roads Administration operates. The wave conditions during experiments were relatively moderate, with significant wave heights generally less than 1.5 m.

Fig. 12. Our data logging system comprises five IMUs, a GPS receiver, a solid state drive, and a synchronization unit.

5.2. Results and discussion

In this section, we present and discuss the results from our PTPD approach when applied to full-scale experimental IMU data. All the wave radar and wave buoy values of the wave direction have been transformed to the wave tangent frame (Fig. 3) to be commensurate with the wave direction estimates given by our algorithm. The wave direction results are shown between 0° and 360° to avoid rapid jumps for values in proximity to 180°. For stationkeeping vessels, the wave number estimate is not particularly interesting as it is implicitly estimated by Algorithm 1 through the peak wave frequency used to generate the desired phase differences (we can use this frequency to calculate the wave number directly based on the dispersion relation for deep waters). For this reason, we consider the wave number redundant and have consequently omitted it from the zero-speed results.

The length and breadth dimensions of Gunnerus are 36.25 m and 9.90 m, respectively. Substituting these values into Eq. (20) with d arbitrarily large (deep waters) yields the maximum frequency threshold $f_{\max} = 0.2$ Hz. The latter value is substituted into Eq. (23) for the forward speed trials to get the adjusted frequency threshold $f_{e,\max}$ when the vessel moves with speed U.

5.2.1. Zero speed

The zero-speed experiments were conducted in two distinct locations (Fig. 11(a)) to assess the performance of our proposed method in two different sea states. Following the sea state code definitions by Price and Bishop (1974), the observed sea states in Location 1 and 2 were moderate and slight, with significant wave heights generally between $1.2 - 1.4$ m and $0.7 - 0.8$ m, respectively. The incident waves in Location 1 are generally larger than Location 2 as they come directly from the open sea, unobstructed by any landmass. In both locations, the swell was heavily dominant compared to the local wind.

Our experimental results (Figs. 15 and 16) show that in both locations, the estimates of the relative wave direction from our proposed method are generally very close to the corresponding values reported by the wave radar and wave buoy systems. Quantitatively, 91% and 71% of the total estimation errors are less than 20° and 10°, respectively, for the physical sensor configuration and, correspondingly, 92% and 70% for the virtual sensor configuration based on a single IMU. In addition to the high accuracy, the similarity of results between the physical and virtual sensor configurations further demonstrates that only a single IMU is indeed sufficient, thus rendering multiple physical IMUs redundant. This important result significantly increases the practical usefulness of our proposed method in addition to being accurate, cheap, portable, flexible, easy to install, and robust against various environmental conditions. In contrast, de facto standard wave buoy and wave radar systems are expensive and suffer from either being geographically confined, less flexible to changes, difficult to install (without expert help), and in some cases, sensitive to the external environment. For instance, during data collection, there were several losses from the wave radar due to precipitation and interference with the surrounding landmass (Fig. 16).

We suspect that uncertainties in the phase differences resulting from the FFT are likely one of the main culprits behind some of the observed deviations between the estimation results and the ground truths. By relying on the FFT, a compromise must be made between time and frequency resolution, which, in turn, translates to a compromise between real-time performance and accuracy—both of which must be present for practical feasibility. The compromise is reflected quantitively through the window length and percentage overlap between consecutive data segments, which for the presented results, were chosen after trial and error as 6 min and 50%, respectively. Collectively, these values produce estimate updates every third minute after initialization, which we consider a reasonable compromise between real-time performance and accuracy.

In the results presented, we reduced the frequency threshold to 0.13 Hz, which produced better results (recall that longer wave periods
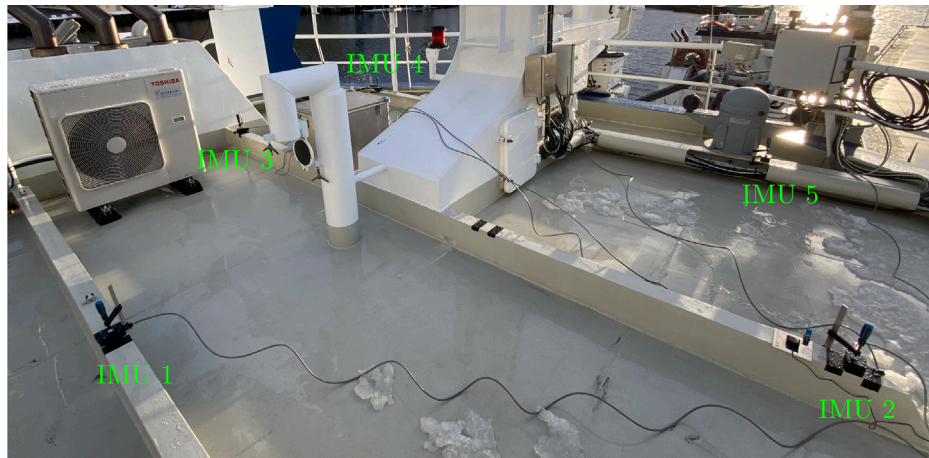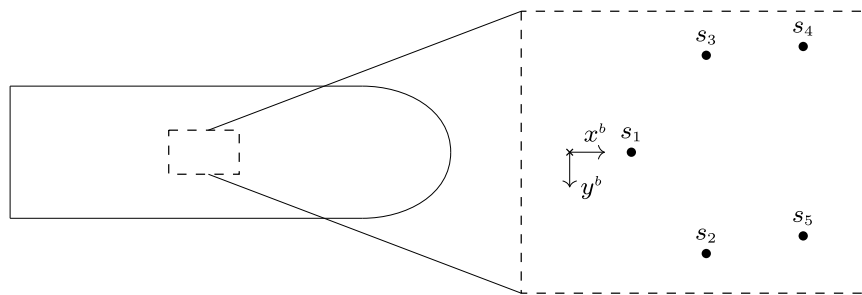
Fig. 13. The IMUs and GPS receiver were clamped to the roof of Gunnerus using screw clamps and connected to the synchronization unit, which was placed downstairs inside the bridge.

[m]	x^b	y^b	z^b
s_1	1.40	-0.02	1.58
s_2	3.12	2.28	1.58
s_3	3.13	-2.23	1.58
s_4	5.29	-2.45	1.58
s_5	5.28	1.87	1.58

Fig. 14. IMU array considered in the full-scale experiments. IMUs 1, 2, 3, 4, and 5 are denoted s_1, s_2, s_3, s_4, and s_5, respectively. The location of each sensor is given in meters with respect to the vessel body frame $\{b\}$. The origin of $\{b\}$ is indicated by a cross, where the z^b-axis (not shown) points down into the page. We have used the same configuration for the virtual sensor locations with IMU 1 considered as the only physical sensor. The virtual measurements from the other "sensors" were obtained by employing the measurement transformation (19) together with the processed linear accelerations, angular rates, and angular accelerations of IMU 1.

generally reduce model mismatch). As discussed in Section 4.2.4, such an adjustment is generally acceptable for unimodal seas where all wave components have the same propagation direction. Indeed, this was the case for both locations, which were largely swell-dominant. However, for a bimodal sea state consisting of swell and local wind-generated waves, our method (if left unmodified) will return the main wave direction and wave number corresponding to the most prominent wave system, assuming the wave systems are clearly distinguishable. This result follows from the current implementation of the method (see Algorithm 3), which assumes a single mode and concludes after finding the frequency associated with the largest peak. It is worth noting that if all the modal frequencies are known, the PTPD approach can be extended to work in multimodal environments by applying the method recursively for each modal frequency. The main challenge, however, is to identify the frequency of each unique mode in the heave acceleration spectrum. The latter can be achieved through various peak detection algorithms such as `findpeaks()` in MATLAB or more advanced techniques based on wavelet analysis (Du et al., 2006).

5.2.2. Forward speed

As mentioned earlier, the forward speed trials were abruptly ended due to ship operational issues shortly after commencing the first trial. For this reason, we consider the only forward speed experiment recorded that day, which lasted approximately 6 min. Despite the short duration, the results (Fig. 17) show great promise—91% of wave encounter angle errors and wave number errors are less than 20° and 0.01 m^{-1}, respectively, for the physical sensor configuration and, correspondingly, 82% and 73% for a single IMU. The wave number errors are particularly interesting as they suggest that it is indeed possible to retain the absolute wave frequency directly while moving with constant forward speed. Unfortunately, we were not able to test the latter in following sea conditions, thereby potentially circumventing the 1-to-3 mapping problem existing between encounter frequency and absolute frequency domains (Nielsen, 2017b, 2018).

6. Conclusions and further recommendations

A relatively new and exciting signal-based approach using the phase-time-path-differences (PTPDs) between a shipboard array of sensors to retrieve directional wave information has been explored in this study. We derived a new kinematic PTPD model accounting for forward vessel speed, thus generalizing the PTPD concept further to moving vessels. The theoretical foundation of this model in terms of modeling sensor delays on a rigid body was carefully assessed, and it was shown
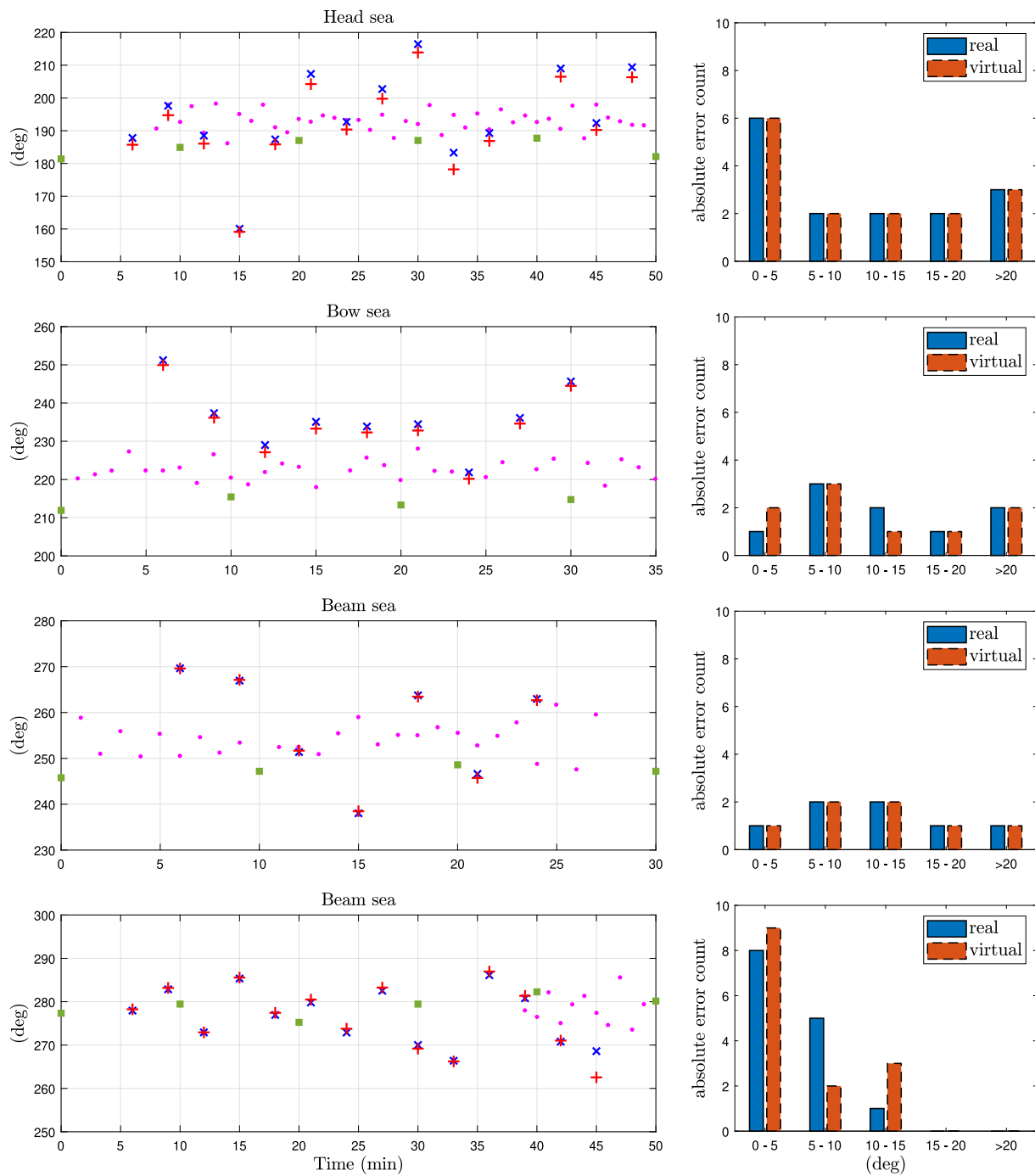
Fig. 15. Relative wave direction estimation results from our wave algorithm (Algorithm 3) from Location 1 (moderate sea with significant wave heights $1.2 - 1.4$ m and water depth 339 m) for four different boat headings corresponding to head, bow, and beam seas. The estimates from the physical sensor configuration are indicated by crosses (blue), whereas the estimates from the virtual sensor configuration based on IMU 1 (Fig. 14) are indicated by plus signs (red). The corresponding wave direction values reported by the wave radar and wave buoy D are represented by dots (pink) and squares (green), respectively. The histograms next to each plot show the corresponding absolute error count for different error intervals for both sensor configurations (real and virtual). The wave radar values are considered as ground truth except for the bottom plot where it was mistakenly off and turned on again after 39 min. Hence, until 36 min, the wave buoy values were considered as reference. For each wave direction estimate (cross or plus sign), comparison was made with the ground truth by considering the value closest in time. All wave directions are given between $[0°, 360°)$ as the positive counterclockwise angle from the x-axis of the wave tangent frame to the vessel body x^b axis (Fig. 3). The window size, segment overlap, and frequency threshold f_{max} were set to 6 min, 50%, and 0.13 Hz, respectively.

that the model's accuracy relies on sufficiently short sensor separations and sufficiently long waves. Based on this theory and PTPD model, we proposed a methodology to resolve the wave propagation direction and wave number online from an array of IMUs and a single IMU by employing a rigid body measurement transform, an FFT, and a UKF. Our methodology incorporates a novel frequency threshold based on the main ship dimensions to avoid distorted wave components caused by vessel lowpass filtering. The wave estimation capabilities of our

proposed method were tested on IMU data collected from a wave tank and full-scale experiments involving a research vessel equipped with a commercial wave radar operating in the proximity of several wave buoys outside the coast of Norway. The estimation results generally agreed very well with the reference wave values reported from both wave measurement systems, demonstrating that a single physical IMU is sufficient. Together, these results significantly increase the practical utility of the PTPD approach, rendering it a serious contender to other
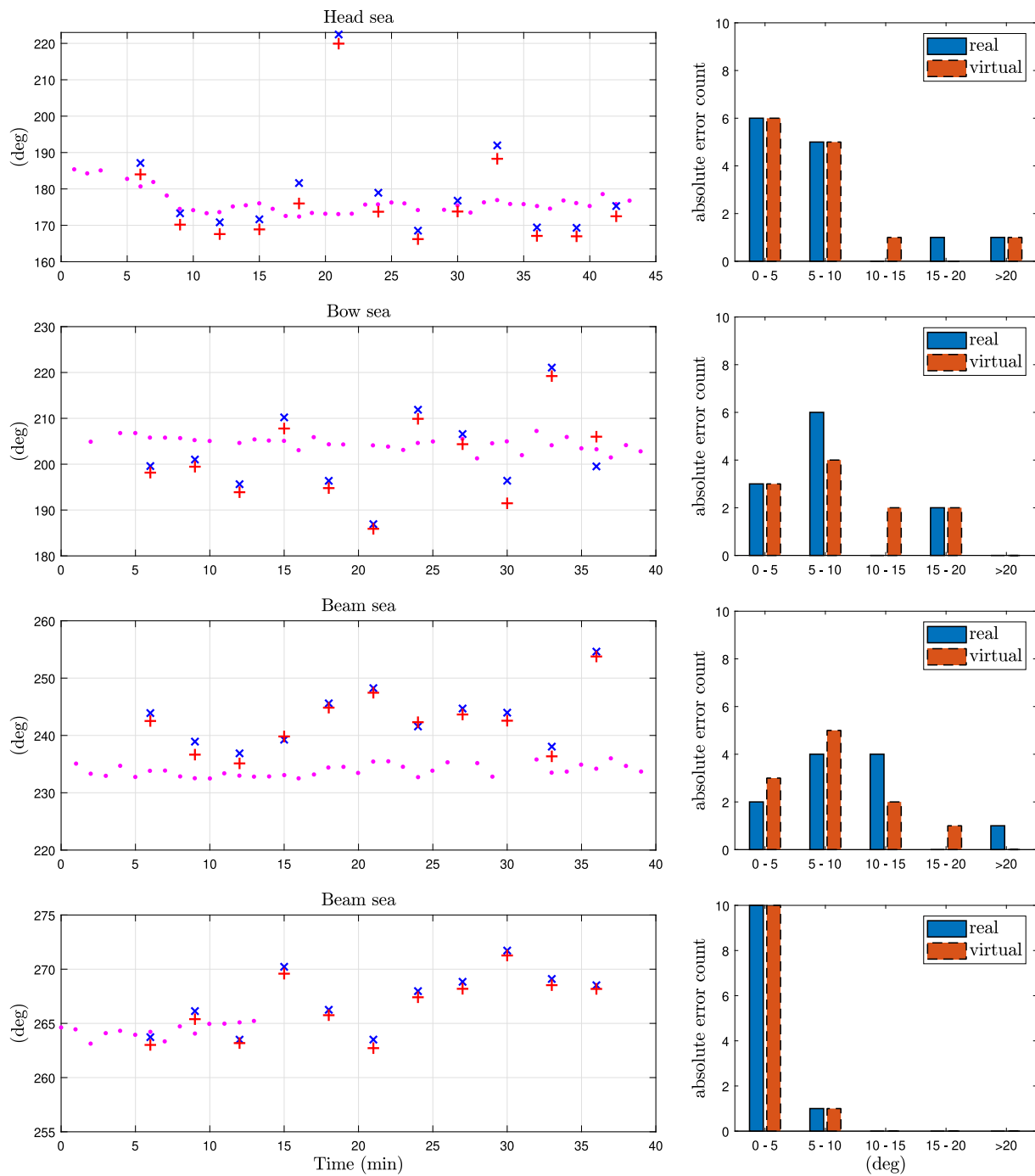
Fig. 16. Relative wave direction estimation results from our wave algorithm (Algorithm 3) from Location 2 (slight sea with significant wave heights $0.7 - 0.8$ m and water depth 442 m) for four different boat headings corresponding to head, bow, and beam seas. The estimates from the physical sensor configuration are indicated by crosses (blue), whereas the estimates from the virtual sensor configuration based on IMU 1 (Fig. 14) are indicated by plus signs (red). The corresponding wave direction values reported by the wave radar are represented by dots (pink). The histograms next to each plot show the corresponding absolute error count for different error intervals for both sensor configurations (real and virtual). For each wave direction estimate (cross or plus sign), comparison was made with the wave radar by considering the value closest in time. In the bottom plot, the wave radar dropped out due to significant interference with the surrounding landmass. For this reason, the remaining comparison with the other wave estimates was made based on the last recorded wave radar value. All wave directions are given between $[0°, 360°)$ as the positive counterclockwise angle from the x-axis of the wave tangent frame to the vessel body x^b axis (Fig. 3). The window size, segment overlap, and frequency threshold f_{max} were set to 6 min, 50%, and 0.13 Hz, respectively.

shipboard signal-based approaches in terms of accuracy and online performance while being cheap, flexible, easy to install, and robust against environmental influences.

As hinted in Section 5.2.1, our wave estimation procedure is currently limited by the FFT, which forces a trade-off between real-time performance and accuracy. In order to increase practical utility further, future studies should seek to optimize the estimation procedure by considering alternative methods to the FFT that are less stringent on

the trade-off above. In this regard, there are, in particular, two approaches worth examining in greater detail, namely, the Hilbert-Huang transform (HHT) and a real-time phase difference tracking filter (Chen et al., 2019). The former approach can yield instantaneous frequency and phase information for non-stationary data, whereas the latter yields the same information in real time but is based on a single sinusoid. A comparison between these approaches (and potential others) and the FFT is left as an application for further studies.
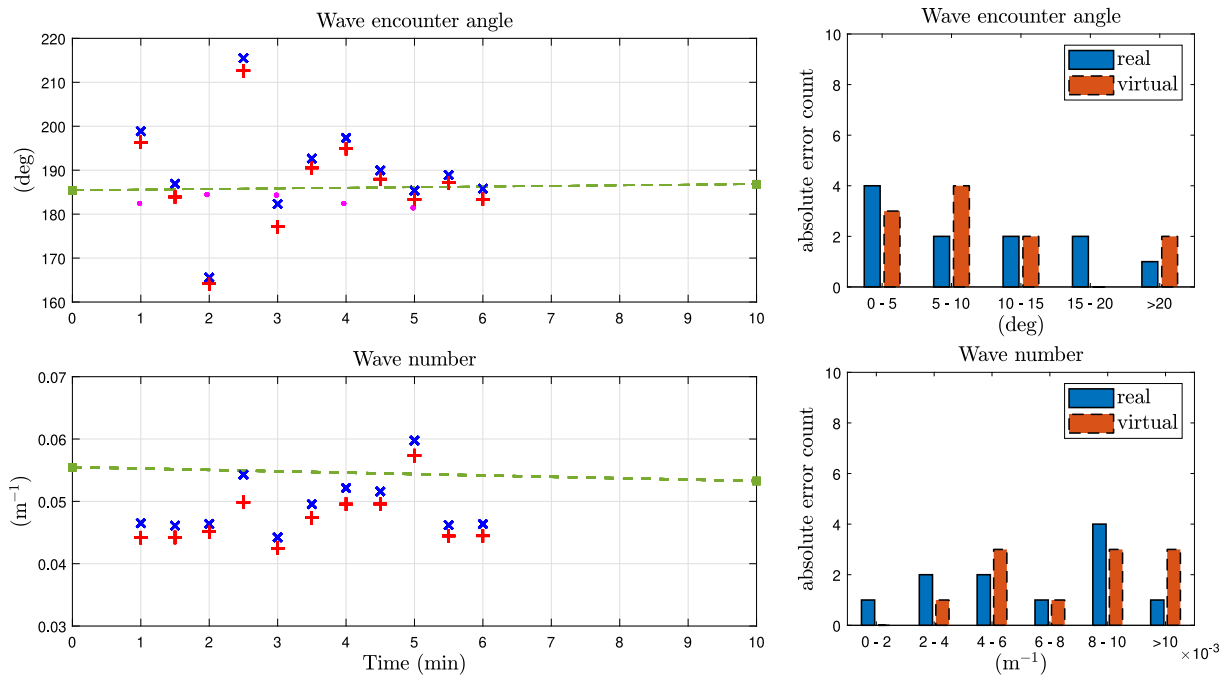
Fig. 17. Relative wave encounter angle and wave number estimation results from our wave algorithm (Algorithm 3) in head sea (moderate sea with significant wave height ∼ 1.3 m and water depth 439 m) with forward vessel speed $U = 10.8$ knots (Fig. 11(b)). The estimates from the physical sensor configuration are indicated by crosses (blue), whereas the estimates from the virtual sensor configuration based on IMU 1 (Fig. 14) are indicated by plus signs (red). The corresponding wave direction values reported by the wave radar and wave buoy (A and D) are represented by dots (pink) and squares (green), respectively. The buoys A and D report the same wave direction and low frequency mean wave period, which has been converted to wave numbers using the dispersion relation (21) for deep waters, and are shown as squares (green) in the wave number plot. The histograms next to each plot show the corresponding absolute error count for different error intervals for both sensor configurations (real and virtual). The wave radar and wave buoy values are considered reference for the wave encounter angle and wave number, respectively. For each wave estimate (cross or plus sign), comparison was made with the ground truth by considering the value closest in time. A dashed line has been extended between the wave buoy values to make comparison easier. All wave directions are given between $[0°, 360°)$ as the positive counterclockwise angle from the x-axis of the wave tangent frame to the vessel body x^b axis (Fig. 3). The window size and segment overlap were set to 1 min and 50%, respectively. The frequency threshold was selected as the maximum default value based on the vessel length and beam dimensions.

The results from the forward speed trials presented in this work are promising but limited from further generalization due to the size of the wave basin (inhibiting other heading angles from being tested) and operational issues onboard RV Gunnerus. For this reason, future investigations should aim for additional forward speed testing in head, bow, beam, quartering, and following sea conditions to further validate our theory and proposed methodology. In particular, additional experimentation in beam to following seas is of interest to show that our approach can directly obtain the absolute true wave frequency, thereby circumventing the 1-to-3 mapping problem generally existing between the encounter and absolute frequency domains.

One of the conditions for the PTPD approach to model sensor delays on a rigid body is that the sensor separations be sufficiently close. However, a too-small sensor separation combined with the (fixed and finite) sensor sampling rate increases the risk of all measured phase differences becoming zero, resulting in a loss of observability of our state-space model. This phenomenon can happen for any given sensor configuration, provided that the propagation speed of the considered waves is sufficiently high. Hence, what constitutes a minimal sensor separation depends on the wave conditions, and finding a lower bound on the separation distance for all situations is difficult. We leave this as a potential topic for future inquiry.

In this study, the primary wave environment considered for practical assessment of the PTPD approach has been long-crested irregular waves. It is important to note that the PTPD method can be extended to work in more short-crested wave environments featuring multiple modes by recursively applying the method to each modal frequency. Identifying these modal frequencies, for instance through various peak detection algorithms based on wavelet analysis, is beyond the scope of the present study.

CRediT authorship contribution statement

Johann A. Dirdal: Conceptualization, Methodology, Software, Validation, Investigation, Formal analysis, Writing, Visualization. **Roger Skjetne:** Conceptualization, Writing – review & editing, Co-supervision. **Jan Roháč:** Conceptualization, Writing – review & editing. **Thor I. Fossen:** Conceptualization, Writing – review & editing, Supervision.

Declaration of competing interest

The authors declare that they have no known competing financial interests or personal relationships that could have appeared to influence the work reported in this paper.

Data availability

Data will be made available on request.

Acknowledgments

Appendix. Model error analysis

In this section, the model deviations between the time-varying and average phase difference models, (11) and (12), respectively, are quantitatively assessed for different wave parameters and roll-pitch
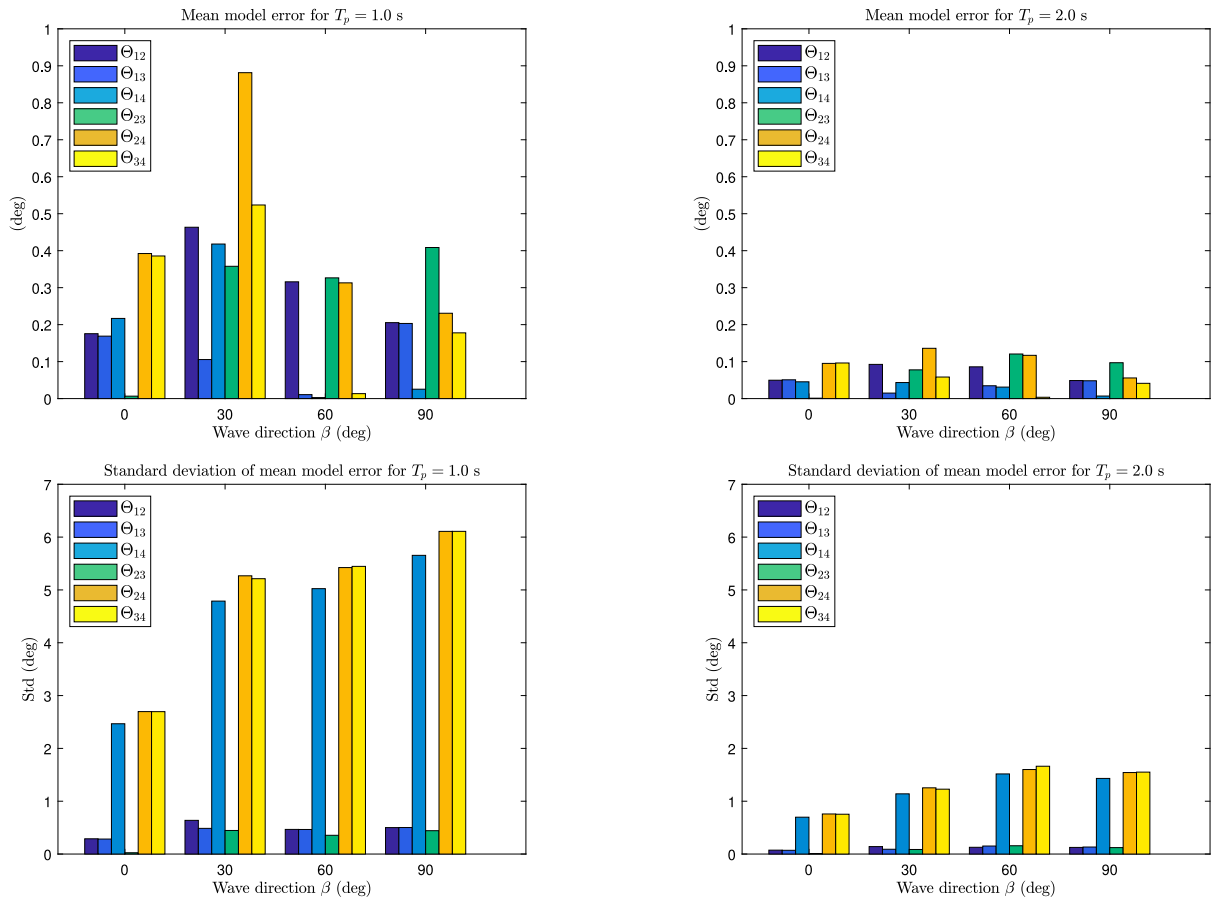
Fig. A.18. For each experimental wave period T_p and wave direction β, the absolute value of the mean error (top) and corresponding standard deviation (bottom) for all phase differences are shown in different colors. The mean error is computed by $1/N \sum ((11)-((12)))$ for a total of N roll and pitch samples based on the sensor configuration in Fig. 6(a), which for four sensors yields a total of six independent phase differences $\{\Theta_{12}, \Theta_{13}, \Theta_{14}, \Theta_{23}, \Theta_{24}, \Theta_{34}\}$. In all experiments, the roll and pitch response amplitudes were scaled to simulate the worst-case conditions of the pool experiments in Section 4. For $\beta = 0°$, the pitch response amplitude was scaled to 5° and, for $\beta = 90°$, the roll response amplitude was scaled to 10°. For $\beta = 30°$ and 60°, both the roll and pitch responses were scaled to 10° and 5°, respectively.

responses. To carry out such an assessment, we consider roll and pitch data from a model ship in regular waves with periods $\{1.0\,\text{s}, 2.0\,\text{s}\}$ and relative wave directions $\{0°, 30°, 60°, 90°\}$. The roll and pitch responses have been scaled to even larger amplitudes to see how increasingly rougher seas may impact the model differences. As we shall see, the model deviations are directly affected by the vessel roll and pitch offset, the height separation between the sensors onboard, and the period of the waves passing through the vessel. The experimental data considered in this analysis were collected as part of the Master's thesis of Udjus (2017).

A.1. Simulation results

The simulation results (Fig. A.18) show the total mean error between Eqs. (11) and (12) and the corresponding standard deviation computed from each roll-pitch sample for the duration of the considered responses. In the computation of these errors, the sensor configuration in Fig. 6(a) was considered, which consists of four sensors and gives access to a total of six independent phase differences in each experiment. The wave number was computed through the dispersion relation in (21), assuming a water depth of 1.5 m.

The following observations are made from the mean model errors and standard deviations in Fig. A.18:

(i) The mean model error for each phase difference is less than 1° for all experiments.

(ii) The standard deviation of each phase difference associated with sensor 4 is significantly larger than the rest.

(iii) The mean model error and standard deviation decrease for increasing wave periods.

Observations (i) and (ii) are discussed in the subsequent subsections, respectively. The downscaling effect (iii) is caused by the wave number k, which is inversely proportional to the wave period. Hence, longer waves imply smaller errors than shorter waves and vice versa.

A.2. Roll and pitch asymmetry

Regarding (i), we repeated the same simulations with roll and pitch responses scaled to 30° and 10°, respectively, and observed similar results (i.e., all errors were less than 1°). These results show that the average phase difference model is more or less independent of roll-pitch amplitude, thus eliminating the need for the small-angle assumption considered in our previous work (Dirdal et al., 2022).

However, if the roll and pitch responses can be asymmetric (e.g., due to uneven loading conditions and/or manufacturing errors), the average roll and pitch angles may no longer be centered close to zero (i.e., $\bar{\phi}(t) = \phi_0 \neq 0$ and $\bar{\theta}(t) = \theta_0 \neq 0$). If these offsets are left unaccounted for, they may cause a bias between the considered phase difference models (Fig. A.19). However, if the roll and pitch offsets are known, the deviation can be alleviated by inserting these values into Eq. (11) and applying this average model instead.
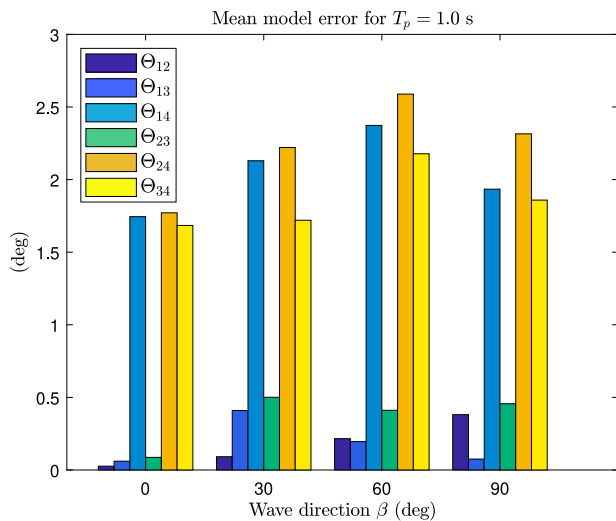
Fig. A.19. Repeated mean model error simulation for wave period $T_p = 1.0$ s (Fig. A.18) but with an offset value of 2° added to all roll and pitch responses.

A.3. Sensor height separation

A significant sensor height separation will amplify any differences between the considered phase difference models due to the latter term in the RHS of Eq. (11). When the roll and pitch responses are symmetric about zero, this amplification effect is manifested mainly in the standard deviations of mean model errors (Fig. A.18). However, if the roll and pitch responses are asymmetric about zero, the sensor height separation may also influence the mean model error (Fig. A.19). This amplification effect can be mitigated by only considering coplanar sensor measurements (i.e., all sensors on the same plane).

References

Brodtkorb, A.H., Nielsen, U.D., Sørensen, A.J., 2018. Sea state estimation using vessel response in dynamic positioning. Appl. Ocean Res. 70.

Brown, R.G., Hwang, P.Y.C., 1997. Introduction to Random Signals and Applied Kalman Filtering: With MATLAB Exercises and Solutions, third ed. Wiley, New York, NY, URL: https://cds.cern.ch/record/680442.

Chen, N., Fan, S., Zheng, D., 2019. A phase difference measurement method based on strong tracking filter for Coriolis mass flowmeter. Rev. Sci. Instrum. 90 (7).

de Souza, F.L., Tannuri, E.A., de Mello, P.C., Franzini, G., Mas-Soler, J., Simos, A.N., 2018. Bayesian estimation of directional wave-spectrum using vessel motions and wave-probes: Proposal and preliminary experimental validation. J. Offshore Mech. Arct. Eng. 140 (4).

Dirdal, J.A., Skjetne, R., Roháč, J., Fossen, T.I., 2022. Online wave direction and wave number estimation from surface vessel motions using distributed inertial measurement arrays and phase-time-path-differences. Ocean Eng. 249.

Dishan, H., 1995. Phase error in fast Fourier transform analysis. Mech. Syst. Signal Process. 9 (2).

Donelan, M.A., Drennan, W.M., Magnusson, A.K., 1996. Nonstationary analysis of the directional properties of propagating waves. J. Phys. Oceanogr. 26 (9).

Draycott, S., Davey, T., Ingram, D.M., Day, J.L.a., Johanning, L., 2015. Using a phase-time-path-difference approach to measure directional wave spectra in FloWave. In: EWTEC Conference Proceedings. pp. 1–7.

Draycott, S., Davey, T., Ingram, D.M., Day, A., Johanning, L., 2016. The SPAIR method: Isolating incident and reflected directional wave spectra in multidirectional wave basins. Coast. Eng. 114, 265–283.

Draycott, S., Noble, D.R., Davey, T., Bruce, T., Ingram, D.M., Johanning, L., Smith, H.C., Day, A., Kaklis, P., 2018. Re-creation of site-specific multi-directional waves with non-collinear current. Ocean Eng. 152.

Du, P., Kibbe, W.A., Lin, S.M., 2006. Improved peak detection in mass spectrum by incorporating continuous wavelet transform-based pattern matching. Bioinformatics 22 (17).

Duz, B., Mak, B., Hageman, R., Grasso, N., 2019. Real time estimation of local wave characteristics from ship motions using artificial neural networks. In: 14th Int. Conf. of Practical Design of Ships and Other Floating Structures. Yokohama, Japan.

Esteva, D.C., 1976. Wave direction computations with three gage arrays. In: Proc. Fifteenth Coastal Engng. Conf., Vol. 1. Hawaii Univ., U.S.A.: Jul. 11–17, 1976, pp. 349–367, New Yo.

Esteva, D.C., 1977. Evaluation of the Computation of Wave Direction with Three-Gauge Arrays. Technical Report, CERC, Technical Paper No. 77-7, U.S. Army Corps of Engineers.

Fernandes, A.A., Gouveia, A.D., Nagarajan, R., 1988. Determination of wave direction from linear and polygonal arrays. Ocean Eng. 15 (4), 345–357.

Fernandes, A.A., Menon, H.B., Sarma, Y.V., Jog, P.D., Almeida, A.M., 2001. Wavelength of ocean waves and surf beat at duck from array measurements. In: Proceedings of the International Symposium on Ocean Wave Measurement and Analysis, Vol. 2.

Fernandes, A.A., Sarma, Y.V., Menon, H.B., 2000. Directional spectrum of ocean waves from array measurements using phase/time/path difference methods. Ocean Eng. 27 (4), 345–363.

Fossen, T.I., 2021. Handbook of Marine Craft Hydrodynamics and Motion Control, second ed. Wiley, Chichester, West Sussex, U.K.

Fu, T.C., Fullerton, A.M., Hackett, E.E., Merrill, C., 2011. Shipboard measurement of ocean waves. In: Proceedings of the International Conference on Offshore Mechanics and Arctic Engineering - OMAE, Vol. 6.

Furevik, B.R., Lønseth, L., Borg, A.L., Neshaug, V., Gausen, M., 2016. Oceanographic observations for the coastal highway E39 project in mid Norway. http://dx.doi.org/10.21343/ef2d-jp97.

Han, P., Li, G., Skjong, S., Zhang, H., 2022. Directional wave spectrum estimation with ship motion responses using adversarial networks. Mar. Struct. 83.

Heyn, H.M., Udjus, G., Skjetne, R., 2017. Distributed motion sensing on ships. In: OCEANS 2017 - Anchorage, Vol. 2017-January.

Holthuijsen, L.H., 2007. Waves in Oceanic and Coastal Waters. Cambridge University Press.

Julier, S., Uhlmann, J., 2004. Unscented filtering and nonlinear estimation. Proc. IEEE 92 (3).

Kandepu, R., Imsland, L., Foss, B.A., 2008. Constrained state estimation using the unscented Kalman filter. In: 2008 Mediterranean Conference on Control and Automation - Conference Proceedings. MED'08'.

Kim, D.H., Kim, N., 2014. An auto weather-vaning system for a DP vessel that uses a nonlinear controller and a disturbance observer. Int. J. Nav. Archit. Ocean Eng. 6 (1).

Kjerstad, O.K., Skjetne, R., 2016. Disturbance rejection by acceleration feedforward for marine surface vessels. IEEE Access 4.

Luo, L., Liu, S., Li, J., Jia, W., 2020. Deterministic reconstruction and reproduction of multi-directional irregular waves based on linear summation model. Ocean Eng. 198, 106952.

Mak, B., Düz, B., 2019. Ship as a wave buoy: Using simulated data to train neural networks for real time estimation of relative wave direction. In: Proceedings of the International Conference on Offshore Mechanics and Arctic Engineering - OMAE, Vol. 9.

Mittendorf, M., Nielsen, U.D., Bingham, H.B., Storhaug, G., 2022. Sea state identification using machine learning—A comparative study based on in-service data from a container vessel. Mar. Struct. 85.

Mounet, R.E., Nielsen, U.D., Brodtkorb, A.H., Tannuri, E.A., de Mello, P.C., 2022. Simultaneous sea state estimation and transfer function tuning using a network of dynamically positioned ships. Appl. Ocean Res. 129.

Nielsen, U.D., 2006. Estimations of on-site directional wave spectra from measured ship responses. Mar. Struct. 19 (1).

Nielsen, U.D., 2007. Response-based estimation of sea state parameters - influence of filtering. Ocean Eng. 34 (13).

Nielsen, U.D., 2008. The wave buoy analogy - estimating high-frequency wave excitations. Appl. Ocean Res. 30 (2).

Nielsen, U.D., 2017a. A concise account of techniques available for shipboard sea state estimation. Ocean Eng. 129.

Nielsen, U.D., 2017b. Transformation of a wave energy spectrum from encounter to absolute domain when observing from an advancing ship. Appl. Ocean Res. 69.

Nielsen, U.D., 2018. Deriving the absolute wave spectrum from an encountered distribution of wave energy spectral densities. Ocean Eng. 165.

Nielsen, U.D., Brodtkorb, A.H., Sørensen, A.J., 2019. Sea state estimation using multiple ships simultaneously as sailing wave buoys. Appl. Ocean Res. 83.

Nielsen, U.D., Dietz, J., 2020. Estimation of sea state parameters by the wave buoy analogy with comparisons to third generation spectral wave models. Ocean Eng. 216.

Nielsen, U.D., Mounet, R.E., Brodtkorb, A.H., 2021. Tuning of transfer functions for analysis of wave–ship interactions. Mar. Struct. 79.

Pascal, R., Lucas, J., Ingram, D., Bryden, I., 2009. Assessing and improving the Edinburgh curved wave tank. In: Proceedings of the International Offshore and Polar Engineering Conference.

Price, W., Bishop, R., 1974. Probabilistic Theory of Ship Dynamics. Chapman and Hall, London.

Simon, D., 2010. Kalman filtering with state constraints: A survey of linear and nonlinear algorithms. IET Control Theory Appl. 4 (8).

Tannuri, E.A., Sparano, J.V., Simos, A.N., Da Cruz, J.J., 2003. Estimating directional wave spectrum based on stationary ship motion measurements. Appl. Ocean Res. 25 (5).

Udjus, G., 2017. Force Field Identification and Positioning Control of an Autonomous Vessel using Inertial Measurement Units (MSc thesis). Norwegian University of Science and Technology, Trondheim, p. 85.

Waals, O.J., Aalbers, A.B., Pinkster, J.A., 2002. Maximum likelihood method as a means to estimate the directional wave spectrum and the mean wave drift force on a dynamically positioned vessel. In: Proceedings of the International Conference on Offshore Mechanics and Arctic Engineering - OMAE, Vol. 4.

Zappa, B., Legnani, G., Van Den Bogert, A.J., Adamini, R., 2001. On the number and placement of accelerometers for angular velocity and acceleration determination. J. Dyn. Syst. Meas. Control Trans. ASME 123 (3).